Author(s): Mahajan, Shreya; Marttinen, Antti; Forsblom, Samu; Lahtinen, Manu

Title: Inorganic Anion-Mediated Supramolecular Entities of 4-Amino-3,5-Bis(4-Pyridyl)-1,2,4-Triazole Salts Assisted by the Interplay of Noncovalent Interactions

Year: 2023

Version: Published version

Please cite the original version:

Mahajan, S., Marttinen, A., Forsblom, S., & Lahtinen, M. (2023). Inorganic Anion-Mediated Supramolecular Entities of 4-Amino-3,5-Bis(4-Pyridyl)-1,2,4-Triazole Salts Assisted by the Interplay of Noncovalent Interactions. Crystal Growth and Design, 23(7), 5144-5162. https://doi.org/10.1021/acs.cgd.3c00393

CRYSTAL GROWTH & DESIGN

pubs.acs.org/crystal

Article

Inorganic Anion-Mediated Supramolecular Entities of 4-Amino-3,5-Bis(4-Pyridyl)-1,2,4-Triazole Salts Assisted by the Interplay of Noncovalent Interactions

Shreya Mahajan, Antti Marttinen, Samu Forsblom, and Manu Lahtinen*

Cite This: *Cryst. Growth Des.* 2023, 23, 5144−5162

Read Online

ACCESS | Metrics & More | Article Recommendations | Supporting Information

ABSTRACT: The development of new families of synthetic molecular systems projecting neutral, bi-, or multi-H-bonding donor units is significant to acquire the desired selectivity within the fascinating area of anion recognition. Here, we illustrate the reaction between a neutral 4-amino-3,5-bis(4-pyridyl)-1,2,4-triazole ligand (**L**) with acidic solutions containing either chloride, bromide, nitrate, phosphate, iodide, sulfate, hexafluorosilicate, fluoride, tetrafluoroborate or perchlorate anions, yielding 16 new anion-mediated supramolecular entities, H_2LCl_2 (**1**), H_2LBr_2 (**2**), $H_2L(NO_3)_2$ (**3**), $HL(H_2PO_4)$ (**4**), $H_2L(H_2PO_4)_2$ (**5**), $[H_2L]_2I_4$ (**6**), $H_2L(NO_3)_2$ (**7**), $H_2L(SO_4)\cdot H_2O$ (**8**), H_2LSiF_6 (**9**), $H_2LSiF_6\cdot 2H_2O$ (**10**), $H_2L(HF_2)_2$ (**11**), H_3LI_3 (**12**), $H_3L(BF_4)_3$ (**13**), $H_3L(ClO_4)_3$ (**14**), $H_3L(ClO_4)_3\cdot 2H_2O$ (**15**), and $H_3LH_3O(SiF_6)_2\cdot 2H_2O$ (**16**), thoroughly examined by elemental analyses, Fourier transform-attenuated total reflectance-infrared (FT-ATR-IR), thermal analysis, powder diffraction, and single-crystal X-ray diffraction. We identified the propensity of $H_2PO_4^-$ into a cyclic hexameric cluster $(H_2PO_4^-)_6$ stabilized by a bent ligand **L** via a combination of functionalities such as an amino group, pyridyl terminals, and a triazolyl core. Additionally, we also found the anion−water clusters ranging from a cyclic tetramer $[(SO_4)_2-(H_2O)_2]^{4-}$ and an octameric cluster $[(SiF_6)_4-(H_2O)_4]_\infty^{8-}$ to an acyclic tetramer $[(ClO_4^-)_2(H_2O)_2]$. As shown by the study, subtle modulation in the crystallization environment offers the possibility to yield entirely distinctive forms of molecular salts comprising both anhydrous and a few hydrates with different protonated numbers (mono-, di- or triprotonated). A systematic study indicates that the molecular salts obtained from different anions construct diverse supramolecular extended architectures (e.g., bricklayer, columns, zig-zag, stair-steps, wave-like, helical, double chain, and criss-cross orientation) self-assembled by a combination of noncovalent interactions, constituting distinct H-bonded geometry patterns, essentially depending on the molecular conformation of the bent ligand and the type of the anion utilized (linear, spherical, triangular, tetrahedral, and octahedral) in the preparation of salts.

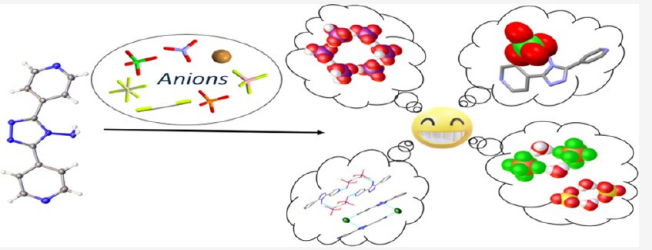

1. INTRODUCTION

The importance of noncovalent interactions in supramolecular assemblies has been well acknowledged and widely demonstrated in the elaboration of supramolecular entities in many scientific disciplines, such as environmental, biological, chemical, and materials sciences to name a few.[1−5] Under noncovalent interactions, hydrogen bonding remains famous and the most reliable, together with other weak forces such as cation−π,[6] anion−π,[7] $\pi-\pi$ stacking interactions,[8] and halogen bonding,[9] which have procured augmented consideration in the field of supramolecular chemistry.

The coexistence of such noncovalent interactions plays a vital role in anion-binding properties and the construction of supramolecular assemblies. Anion binding has attracted continued interest because of the pertinent role performed by anions in biological, chemical, and environmental processes.[10−12] From a structural perspective, it is well known that anions may perform diverse roles during crystallization processes, which include anions acting as a building unit, a secondary building unit (SBU) component, a templating agent, or as a spectator solely for charge balance.[13] The resulting assemblies can essentially be governed by the nature and a wide spectrum of geometries available for inorganic anions ranging from linear ($[HF_2]^-$), spherical (Cl^-, Br^-, I^-), trigonal planar ($[NO_3]^-$), and tetrahedral ($[ClO_4]^-$, $[SO_4]^{2-}$, $[H_2PO_4]^-$, $[BF_4]^-$) to octahedral ($[SiF_6]^{2-}$) geometries.

Within the intrinsic anion chemistry in aqueous media, anion−water clusters hold special interest, as a wide array of structures encompassing a cyclic tetramer, a pentamer, a hexamer, and an octamer can be generated, which are

Received: March 31, 2023
Revised: May 26, 2023
Published: June 23, 2023

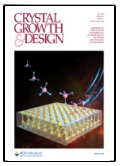

https://doi.org/10.1021/acs.cgd.3c00393
Cryst. Growth Des. 2023, 23, 5144−5162

predominantly controlled by noncovalent interactions being regulated from the surrounding ligand.[14] Likewise, of all of the oxyanion species, phosphates especially possess a natural propensity to undergo self-aggregation to form anion assemblies, i.e., "anion clusters", as reported in the literature.[15−17] Indeed, phosphate recognition by receptors has received tremendous attention owing to its substantial influence on biological and physiological systems.[18] Hence, understanding such interanionic interactions is an interesting challenge and is now considered a critical area of supramolecular focus.[19−21] Nevertheless, supramolecular chemists have devoted tremendous efforts toward understanding and recognizing the serious concerns induced by anions, and substantial development have been accomplished in the range of fields as distinct as anion transport, sensing, extraction, organocatalysts, and so forth.[22−24] Subsequently, new families of synthetic molecular systems projecting neutral, bi-, or multi-H-bonding donor units have emerged in the literature to acquire the desired selectivity within the fascinating area of anion recognition.[4,12,25,26]

Alongside these well-preorganized synthetic receptors outspread in the field of supramolecular chemistry, the chemistry of bis(pyridyl)-based molecules has been the subject of intensive study and has brought new avenues in the construction of elegant supramolecular entities, as aromatic N-comprising supramolecular synthons offer a promising platform to study the interplay of varied noncovalent interactions employed in crystal engineering.[27,28] Ding and coworkers[29] reported anion-assisted supramolecular entities of 2,5-bis(4-pyridyl)-1,3,4-oxadiazole (**4-bpo**), showing structural insights into wide-ranging supramolecular networks manifested by different noncovalent interactions and nature of inorganic anions. To this purpose, we envisioned that the incorporation of a 4-amino-1,2,4-triazole moiety between the two pyridyl groups would be meaningful, as the amino group could serve additional H-bonding sites or feature potential coordination in controlling the formation of final higher-dimensional supramolecular assemblies. With this in mind, we turned our attention to the ligand (**L**, Figure 1), whose capabilities for

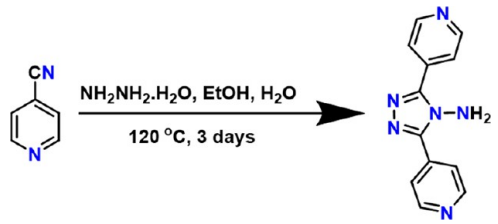

Figure 1. General synthesis route for 4-amino-3,5-bis(4-pyridyl)-1,2,4-triazole (**L**).

spin crossover properties[30−32] and anion−π interactions[33] have been well known. Besides, this bent ligand has been exploited for the construction and design of novel metal−organic frameworks (MOFs)[34−37] and documented independently by the group Du et al.[38] as cocrystals with a series of organic carboxylic acids.

Surprisingly, the research on anion-templated supramolecular assemblies of this ligand remains underexplored. This motivated us in this study to highlight some interesting structural insights into new diverse supramolecular networks constructed by the bent ligand. Examination of **L** encouraged us to ponder over a few points: Will anion's steric effects influence the molecular conformation of **L**? What will be the role of counteranion geometry on H-bonding patterns? Can we attempt to produce salts with mono-, di-, or triprotonated ligands via tuning the acid in different crystallization conditions? Formation of anion or anion−water clusters? Which panel of noncovalent interactions will mediate the molecular packing of the complexes? To address these questions, we launched a systematic analysis on 16 new supramolecular assemblies induced by inorganic anionic species, implying how subtle modulation of distinct noncovalent forces and their dependence on geometries features of anions drive the final formation of supramolecular architectures, the studies of which are submitted in this article.

2. EXPERIMENTAL PROCEDURES

2.1. Materials and Physical Measurements. All of the reagents and solvents were obtained from standard commercial suppliers and utilized as received unless otherwise specified.

2.1.1. Single-Crystal X-ray Diffraction (SCXRD). The diffraction data for the single-crystal structure determination were collected on a Rigaku SuperNova dual-source (Cu and Mo micro-sources) X-ray diffractometer equipped with an Atlas CCD detector and multilayer optics producing monochromatized Cu K_α (1.54187 Å) radiation. The data collection, reduction of datasets, and analytical face-index-based absorption correction methods were carried out using the CrysAlisPRO[39] program. All structures were solved by intrinsic phasing (ShelXT)[40,41] and refined on F^2 by full-matrix least-squares techniques with the ShelXL program in the Olex^2 (v. 1.3 and 1.5) program[42] that utilizes the SHELXL-2013 module.[43] All C−H hydrogen atoms were calculated to their optimal positions and treated as riding atoms using isotropic displacement parameters of 1.2 (sp^2 group) larger than that of the host atom, whereas N−H hydrogen atoms indicating protonation of the ligand or hydrogens of acid groups (e.g., sulfate, phosphate) were primarily found from the electron density maps and were refined freely.

2.1.2. Powder X-ray Diffraction (PXRD). PXRD data were measured using a Panalytical X'Pert PRO diffractometer with Cu K_α radiation (λ = 1.54187 Å; Ni β-filter; 45 kV, 40 mA). Each powder sample was attached to a silicon-made "zero-background signal generating" plate using petrolatum jelly as an adhesive. Diffraction intensities were recorded by an X'Celerator detector at room temperature with a 2θ range of 4−60°, a step size of 0.017°, and a counting time of 70 s per step. Data processing, search-match phase analyses, and Pawley fits were carried out by the program X'pert HighScore Plus (v. 4.9). Search-match phase identification analyses were made against the ICDD-PDF4+ database (version 2020) implemented in the HighScore.[44,45] In the Pawley fits, the unit-cell parameters of the PXRD patterns were refined by using the corresponding single-crystal structure parameters as the basis of least-squares refinement. Variables for the fits were as follows: zero-offset, polynomial background, sample height displacement, unit-cell parameters, and peak profile parameters (peak width, shape, and asymmetry).

2.1.3. Thermal Analysis. The thermal properties of the compounds were examined by a Perkin Elmer STA 6000 thermogravimetric TG/DSC analyzer (DSC stands for a differential scanning calorimetric signal). Each sample was prepared in an open platinum pan and heated under N_2 or air atmospheres (flow rate of 40 mL/min) with a heating rate of 10 °C/min at a temperature range of 22−600 °C. For each run under N_2, a 10 min isotherm at 22 °C was introduced to assure proper purging of the furnace interior from the ambient air atmosphere before the start of the heating. Temperature calibration of the analyzer was made using melting points of the indium (156.6 °C), zinc (419.5 °C), and aluminum (660.3°) standards. The weight balance was calibrated at room temperature using a standard weight of 50.00 mg. The sample weights used in the measurements were about 1.5−14 mg.

https://doi.org/10.1021/acs.cgd.3c00393
Cryst. Growth Des. 2023, 23, 5144−5162

2.2. Other Methods. The ^{1}H NMR and ^{13}C NMR spectra were recorded in $(CD_3)_2SO$ on a Bruker Avance 300 MHz spectrometer. The chemical shifts were reported in ppm relative to CD_3CD_2HSO (δ 2.50) for ^{1}H NMR. For the ^{13}C NMR spectra, $(CD_3)_2SO$ (δ 39.52) was used as an internal standard. All of the FTIR spectra were recorded using a Bruker instrument over a range of 4000−400 cm^{-1}. The samples were mildly ground before pressing a small amount on the diamond ATR Prism and were baseline-corrected. Elemental analyses (C, H, and N) were performed in-house using an Elementar EL III elemental analyzer.

2.3. Syntheses. *2.3.1. Synthesis of 4-Amino-3,5-bis(4-pyridyl)-1,2,4-triazole (bpt).* **L** (bpt) was synthesized according to the reported method with slight modification.[46] 4-Cyanopyridine (2.6 g, 25 mmol), hydrazine monohydrate (79%, 3 mL), water (8 mL), and ethanol (1 mL) were sealed in a Teflon-lined autoclave (25 mL) and heated at 120 °C for 48 h (Figure 1). Slow cooling of the autoclave to 22 °C afforded pale brownish orange crystals. The crystals were isolated by filtration followed by washing with water and acetone and dried in vacuo. Yield = 1.1742 g, 39.4%. Anal. Calc. for **L** $C_{12}H_{10}N_6$: C, 60.50; H, 4.23; N, 35.27. Found: C, 61.34; H, 4.659; N, 34.44%.**^{1}H NMR** (300 MHz, DMSO-d_6): δ 8.79 (d, J = 5.5 Hz, 4H), 8.07 (d, J = 5.6 Hz, 4H), 6.51 (s, 2H). **^{13}C NMR** (75 MHz, DMSO-d_6): δ 153.0, 150.1, 133.9, 122.0. ^{1}H NMR and ^{13}C NMR spectra of a ligand are shown in Figures S1 and S2, respectively.

2.4. Crystallization Methods. *2.4.1. Preparation of H_2LCl_2 (**1**), H_2LBr_2 (**2**), $H_2L(NO_3)_2$ (**3**), $HL(H_2PO_4)$ (**4**), $H_2L(H_2PO_4)_2$ (**5**), $H_2L(SO_4)\cdot H_2O$ (**8**), H_2LSiF_6 (**9**), and $H_2LSiF_6\cdot 2H_2O$ (**10**).* A total of 150 mg of **L** was added to 2 mL of 5 M acid solution (H_2SiF_6 33.5−35%, ∼2.9 M) and shaken thoroughly. After standing undisturbed for 24 h (4 days in the case of salt **9**), single crystals formed in the case of a HNO_3 solution (**3**) were collected and rinsed with water and acetone. To the remaining vials, 2 mL of H_2O was added (except salt **9**), followed by the addition of 8−10 mL of acetone (20 mL of acetone in the case of salt **9**, and dioxane instead of acetone in the case of salt **5**) to precipitate colorless crystals per appropriate LH_x salt (fine powder in case of salt **9**). The solids obtained were filtered, washed with acetone, and air-dried. In the case of **9**, a powder containing a water solution (25 mM) was slowly evaporated to dryness, which afforded crystals suitable for single-crystal X-ray diffraction. The comparison of the FT-ATR-IR (cm^{-1}) of the salts is shown in Figures S3 and S4.

*2.4.1.1. H_2LCl_2 (**1**).* FT-ATR-IR (cm^{-1}): 3159, 3064, 3038, 2967, 2850, 2092, 2051, 2016, 1944, 1895, 1830, 1626, 1588, 1520, 1506, 1483, 1453, 1418, 1364, 1323, 1312, 1287, 1225, 1195, 1182, 1093, 1077, 1051, 1029,1004, 975, 945, 845, 813, 728, 705, 686, 666, 646, 602, 563, 501, 421. Anal. Calc. for $C_{12}H_{12}N_6Cl_2$: C, 46.32; H, 3.887; N, 27.01. Found: C, 46.48; H, 3.769; N, 26.96%.

*2.4.1.2. H_2LBr_2 (**2**).* FT-ATR-IR (cm^{-1}): 3170, 3029, 2936, 2848, 2785, 2166, 2073, 1995, 1926, 1855, 1805, 1627, 1587, 1520, 1506, 1485, 1453, 1418, 1372, 1337, 1323, 1307, 1288, 1272, 1225, 1197, 1186, 1090, 1079, 1051, 1039, 1010, 975, 934, 887, 840, 805, 734, 724, 704, 683, 645, 602, 531, 498, 420. Anal. Calc. for $C_{12}H_{12}N_6Br_2$: C, 36.03; H, 3.023; N, 21.01. Found: C, 35.93; H, 3.107; N, 21.02%.

*2.4.1.3. $H_2L(NO_3)_2$ (**3**).* FT-ATR-IR (cm^{-1}): 3328, 3250, 3111, 3076, 3051, 2630, 2113, 1751, 1627, 1596, 1529, 1518, 1498, 1462, 1392, 1339, 1310, 1294, 1238, 1198, 1127, 1111, 1099, 1086, 1054, 1039, 1006, 994, 979, 949, 886, 836, 821, 736, 719, 688, 665, 649, 602, 531, 508, 473, 418. Anal. Calc. for $C_{12}H_{12}N_8O_6$: C, 39.57; H, 3.320; N, 30.76. Found: C, 39.62; H, 3.324; N, 30.97%.

*2.4.1.4. $H_2L(H_2PO_4)_2$ (**5**).* FT-ATR-IR (cm^{-1}): 3272, 3109, 3061, 2744, 2351, 2164, 1730, 1632, 1516, 1478, 1452, 1362, 1316, 1255, 1094, 1063, 1014, 969, 925, 851, 826, 738, 709, 694, 651, 603, 538, 484, 419. Anal. Calc. for $C_{12}H_{18}N_6O_9P_2$: C, 31.87; H, 4.012; N, 18.58. Found: C, 31.64; H, 3.774; N, 18.80%.

*2.4.1.5. $H_2L(SO_4)\cdot H_2O$ (**8**).* FT-ATR-IR (cm^{-1}): 3478, 3344, 3159, 3036, 2969, 2771, 2163, 2054, 2016, 1939, 1627, 1589, 1520, 1506, 1484, 1454, 1347, 1311, 1242, 1226, 1150, 1092, 1077, 1032, 970, 947, 877, 845, 831, 813, 733, 687, 647, 622, 598, 563, 502, 417. Anal. Calc. for $C_{12}H_{14}N_6O_8S_2$: C, 33.18; H, 3.248; N, 19.35. Found: C, 33.54; H, 3.246; N, 19.32%.

*2.4.1.6. H_2LSiF_6 (**9**).* FT-ATR-IR (cm^{-1}): 3331, 3215, 3086, 2886, 2084, 1632, 1605, 1523, 1505, 1463, 1340, 1309, 1244, 1211, 1098, 984, 956, 829, 735, 724, 690, 659, 636, 601, 529, 507, 473, 418.Anal. Calc. for $C_{12}H_{12}N_6F_6Si$: C, 37.70; H, 3.163; N, 21.98. Found: C, 36.91; H, 3.079; N, 21.98%.

*2.4.2. Preparation of $H_2L(NO_3)_2$ (**7**).* The single crystals formed in the case of the salt (**3**) were dissolved in a 1:1 methanol/water (1 mL) mixture. The faint yellow crystals were afforded within a few days by the slow evaporation of the mixture.

*2.4.3. Preparation of $[H_2L]_2I_4$ (**6**), $H_2L(HF_2)_2$ (**11**), H_3LI_3 (**12**), $H_3L(BF_4)_3$ (**13**), $H_3L(ClO_4)_3$ (**14**), $H_3L(ClO_4)_3\cdot 2H_2O$ (**15**), and $H_3L(H_3O)(SiF_6)_2\cdot 2H_2O$ (**16**).* A total of 150 mg of **L** was added to 2 mL of a 5 M acid solution (H_2SiF_6 33.5−35%, ∼2.9 M) and shaken thoroughly. After standing undisturbed for 24 h, 2 mL of H_2O was added to the iodide salt (**6**) containing solution. All solutions, except salt **15** (closed vial), were left to evaporate in open vials to yield colorless single crystals (red-orange in the case of iodide salts).

*2.4.3.1. $[H_2L]_2I_4$ (**6**).* FT-ATR-IR (cm^{-1}): 3252, 3164, 3090, 3031, 2970, 2910, 2801, 2001, 1916, 1837, 1726, 1625, 1597, 1580, 1510, 1487, 1451, 1363, 1340, 1283, 1239, 1209, 1188, 1100, 1085, 1076, 1051, 1010, 969, 895, 806, 724, 701, 681, 665, 644, 599, 518, 495, 445, 416. Anal. Calc. for $C_{12}H_{12}N_6I_2$: C, 29.17; H, 2.448; N, 17.01. Found: C, 28.94; H, 2.541; N, 17.08%.

*2.4.3.2. $H_2L(HF_2)_2$ (**11**).* FT-ATR-IR (cm^{-1}): 3528, 3333, 3215, 3085, 2885, 1632, 1602, 1525, 1508, 1460, 1363, 1333, 1245, 1214, 1089, 1045, 977, 940, 876, 827, 733, 689, 636, 606, 508, 473, 418. Anal. Calc. for $C_{12}H_{10}N_6$: C, 60.50; H, 4.23; N, 35.27. Found: C, 60.74; H, 4.209; N 34.97%.

*2.4.3.3. $H_3L(BF_4)_3$ (**13**).* FT-ATR-IR (cm^{-1}): 3395, 3271, 3124, 2980, 2905, 1644, 1609, 1556, 1527, 1506, 1481, 1344, 1309, 1292, 1238, 1055, 993, 957, 872, 811, 793, 766, 736, 729, 710, 666, 646, 605, 522, 486, 417. Anal. Calc. for $C_{12}H_{13}N_6F_{12}B_3$: C, 28.73; H, 2.612; N, 16.75. Found: C, 28.98; H, 2.633; N, 17.07%.

*2.4.3.4. $H_3L(ClO_4)_3$ (**14**).* FT-ATR-IR (cm^{-1}): 3376, 3242, 3171, 3112, 2946, 2895, 2791, 2710, 1719, 1643, 1603, 1552, 1523, 1504, 1478, 1412, 1339, 1304, 1235, 1083, 1029, 962, 919, 808, 788, 735, 723, 707, 665, 617, 603, 522, 484, 466. Anal. Calc. for $C_{12}H_{13}N_6O_{12}Cl_3$: C, 26.71; H, 2.428; N, 15.57. Found: C, 26.27; H, 2.534; N, 15.61%.

2.5. Bulk Powder Syntheses. To probe the impact of concentration or pH in the salt formation, the bulk samples were fabricated under three different concentrations (1, 2.5, and 5 M) of acid solutions (HF, HCl, HBr, HI, HNO_3, H_2SO_4, H_3PO_4, HBF_4, $HClO_4$). Note that H_2SiF_6 is an exception, as only 1 and ∼2.9 M were prepared due to the low molarity (33.5−35%, ∼2.9 M) of the commercial acid solution. The complexes were synthesized by adding 150 mg of **L** to 2 mL of different molarity acid solutions and shaking thoroughly. After standing undisturbed for 48 h, 15 mL of acetone was added to precipitate appropriate LH_x salt. The powders obtained (except in the case of $HClO_4$ and HBF_4) were suction filtered, rinsed with acetone, and dried in a desiccator. The remaining vials ($HClO_4$ and HBF_4) were left to evaporate to dryness. The resulting products were collected by filtration and washed with acetonitrile and diethyl ether, respectively, and dried in a desiccator.

3. RESULTS AND DISCUSSIONS

In general, reactions between neutral ligand **L** and selected mineral acids (HCl, HBr, HI, HF, HNO_3, H_3PO_4, H_2SO_4, H_2SiF_6, HBF_4, $HClO_4$) yield either anhydrous or hydrated salts with a di- or triprotonated ligand and the anion(s) corresponding to the acid. The only exception showing a monoprotonated ligand was afforded when the ligand was treated with phosphorus acid in different crystallization conditions.

The reactions generally produced colorless (faint yellow and red-orange in the case of nitrate and iodide salts, respectively) crystals in good to quantitative yields and were readily suitable for single-crystal structure determination without further

https://doi.org/10.1021/acs.cgd.3c00393
Cryst. Growth Des. 2023, 23, 5144−5162

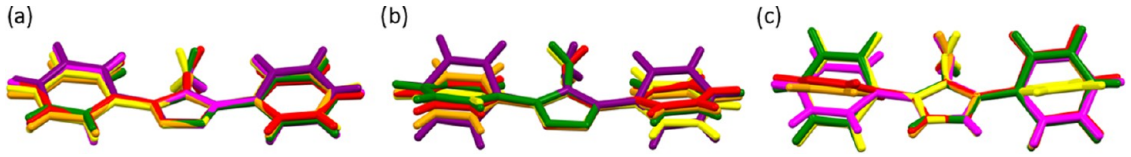

Figure 2. Ligand conformations grouped by their similarity. (a) Group I: (**1**) H_2L chloride (red), (**2**) H_2L bromide (orange), (**3**) H_2L nitrate monoclinic form (yellow), (**4**) HL phosphate (green), (**5**) H_2L phosphate (magenta), and (**6**) $[H_2L]_2$ iodide (purple). (b) Group II: (**7**) H_2L nitrate in triclinic form (red), (**8**) H_2L sulfate (orange), (**9**) H_2L hexafluorosilicate (purple), (**10**) H_2L hexafluorosilicate hydrate (yellow), and (**11**) H_2L bifluoride (green). (c) Group III: (**12**) H_3L iodide (red), (**13**) H_3L tetrafluoroborate (orange), (**14**) H_3L perchlorate (yellow), (**15**) H_3L perchlorate hydrate (green), and (**16**) H_3L hexafluorosilicate (magenta).

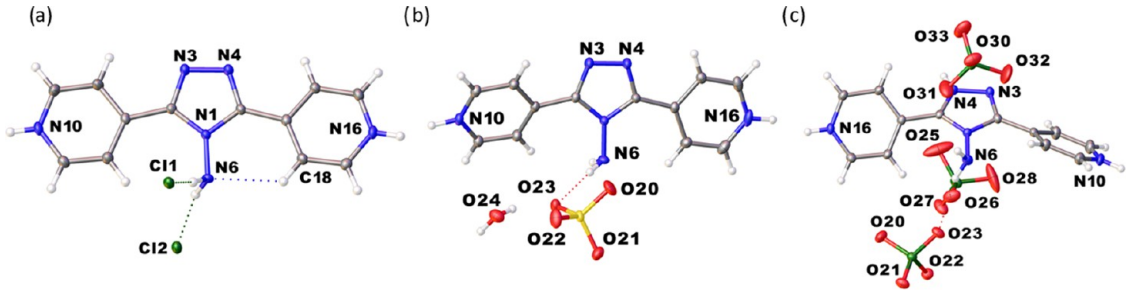

Figure 3. Molecular conformations and the selected atom numbering of (a) group I: H_2LCl_2 (**1**), (b) group II: $H_2L(SO_4)\cdot H_2O$ (**8**), and (c) group III: $H_3L(ClO_4)_3$ (**14**). The atom numbering of the ligand in (a) equals all structures. Weak intramolecular and intermolecular H bonds are exemplified by dashed blue and red (green for chloride salt) colored lines, respectively.

Table 1. Dihedral Angles between Pyridyl Rings and a Central Triazole Ring on Ligand L in Salts (1)−(16)

group I			group II			group III		
comp.	angle 1[a] (deg)	angle 2[b] (deg)	comp.	angle 1[a] (deg)	angle 2[b] (deg)	comp.	angle 1[a] (deg)	angle 2[b] (deg)
1	1.8(2)	−7.3(2)	**7**	16.0(2)	−18.3(2)	**12**	31.4(9)	42.5(9)
2	9.5(3)	−5.2(3)	**8**	−22.22(19)	0.97(18)	**13**	34.08(18)	36.92(18)
3	−11.24(18)	11.44 (18)	**9**	26.9(6)	−13.4(5)	**14**	−35.1(2)	−35.8(2)
4	−0.5(3)	10.8(3)	**10**	27.8(2)	0.4(3)	**15**	37.7(6)	−36.5(6)
5	13.0(2)	−16.1(2)	**11**	22.7(2)	−14.9(2)	**16**	23.9 (2)	−3.4(2)
6	15.5(6)	−15.5(6)						
	13.7(6)[c]	−17.7(6)[d]						

[a]Atoms for the dihedral angles: N3−C2−C7−C12. [b]Atoms for the dihedral angles: N4−C5−C13−C14, for (**6**) [c]Atoms for the dihedral angles: N21−C20−C25−C30 and [d]Atoms for the dihedral angles: N22−C23−C31−C36 for the 2nd ligand in asymmetric unit.

recrystallization, as good quality crystals could be selected directly from the acidic reaction solutions. The structural analysis reveals that the ligand **L** practically adopts (Figure 2) three significantly different molecular conformations, according to which the discussions of the structures are subdivided into future paragraphs. First, the conformational analysis of the ligand is described, followed by the intermolecular interaction and molecular packing analyses of the structures.

3.1. Ligand Conformation Analysis. As shown in Figure 2, group I includes Cl^-, Br^-, I^-, $[NO_3]^-$ (monoclinic structure form), and both $[H_2PO_4]^-$ structures. In all six crystal structures, the ligand shows an almost planar conformation resulting in only very modest dihedral angles between the pyridyl and triazole rings, the highest angles being less than ±17°. In group II (triclinic $[NO_3]^-$, $[SO_4]^{2-}$, both hydrated and anhydrous $[SiF_6]^{2-}$, and F^-), pyridyl groups merely reside on the same plane and are equally tilted from the triazole ring, with angles varying typically between 16 and 27°. Group III contains all triprotonated salts ($[BF_4]^-$, I^-, both $[ClO_4]^-$, $[SiF_6]^{2-}$), wherein one of the pyridyl rings can either be leveled with the central triazole ring and the second pyridyl ring is strongly tilted or both pyridyls are strongly tilted in opposite directions, showing up to 43° dihedral angles in relation to the central triazole ring. For the most tilted ligand conformations, such as in iodide and tetrafluoroborate salts, the pyridyl rings are almost in perpendicular orientation to each other, as shown in Figure 2c.

The six members of group I were obtained by reacting a neutral ligand **L** in acidic water solutions, containing either chloride, bromide, iodide, nitrate, or phosphate anions. All of the formed salts in this group crystallized without solvent molecules in their crystal lattice. Crystallographic data and the selected structure refinement parameters are shown in Table S1, and the asymmetric unit (AU) of the structures of all three groups is available in Figures S5−S7. The selected depictions of AUs per the conformation group are exemplified in Figure 3, and all of the relevant dihedral angles are tabulated in Table 1. In the case of a chloride solution, a diprotonated form of **L**, H_2L^{2+}, was crystallized in triclinic space group *P*-1, giving rise to H_2LCl_2 (**1**) with a single ligand and two chloride anions in the AU. Pyridyl rings of the ligand make dihedral angles of 1.8(2) and −7.3(2)° with the central triazole ring, thus showing close to the planar conformation of the ligand (Figure 3a). In the case of a bromide solution, the diprotonated solvent-free salt H_2LBr_2 (**2**) formed. Similarly to isostructural chloride salt (**1**), the ligand in the bromide salt (**2**) is nearly

https://doi.org/10.1021/acs.cgd.3c00393
Cryst. Growth Des. 2023, 23, 5144−5162

planar, showing only modest dihedral angles (9.5(3) and −5.2(3)°) between pyridyl rings and the central triazole. In the case of a nitrate solution, two different structure modifications were afforded depending on the reaction conditions, of which the monoclinic $P2_1/c$ form $H_2L(NO_3)_2$ (**3**) and the triclinic $P\text{-}1$ form $H_2L(NO_3)_2$ (**7**) belong to the groups I and II, respectively. The monoclinic structure, with a composition of one ligand and two planar nitrate anions, shows dihedral angles of −11.24(18) and 11.44(18)° between the pyridyl and triazole rings, hence having the third least planar ligand geometry within group I. The next two members of group I were cultivated from phosphorus acid solutions and displayed either a mono- or a diprotonated ligand with one or two dihydrogen phosphate anions (**4**, **5**) that crystallized in a monoclinic system with $P2_1/c$ or $I2/a$ symmetries, respectively. For monoprotonated salt (**4**), consisting of a single ligand and a dihydrogen phosphate anion, the dihedral angles between the two pyridine rings and the central triazole ring are 10.8(3) and −0.5(3)°. Whereas for the diprotonated phosphate salt (**5**) with two $[H_2PO_4]^-$ anions, the dihedral angles between the rings are 13.0(2) and −16.1(2)°, thereby showing the second highest tilting of pyridyl rings in this group. In the case of an iodide system, depending on the crystallization conditions, two iodide complexes (**6**, **12**) can be isolated that differ considerably in their molecular conformations despite both the complexes crystallizing in the same triclinic $P\text{-}1$ symmetry. The diprotonated complex $[H_2L]_2I_4$ (**6**) has a somewhat planar ligand, but the triprotonated H_3LI_3 salt (**12**) has a strongly tilted ligand and thereby belongs to group III. The asymmetric unit of (**6**) comprises four iodide anions and two ligand molecules that show dihedral angles of 15.5(6) and −15.5(6)° (13.7(6) and −17.7(6)° for the 2nd ligand) between the pyridyl rings and the triazole core, hence being the least planar ligand in group I.

Molecular salts of group II, namely $H_2L(NO_3)_2$ (**7**), $H_2L(SO_4)\cdot H_2O$ (**8**), H_2LSiF_6 (**9**), $H_2LSiF_6\cdot 2H_2O$ (**10**), and $H_2L(HF_2)_2$ (**11**), were afforded from the reactions between a neutral ligand **L** and acid solutions containing either nitrate, sulfate, hexafluorosilicate, or fluoride anions, respectively. The structures of salts (**8**) and (**10**) crystallized with solvent molecules in their crystal lattice. The dihedral angles for this group are provided in Table 1, and the crystal structures are shown in Figure S6. $H_2L(NO_3)_2$ (**7**), crystallizes in triclinic space group $P\text{-}1$ with one ligand and two planar nitrate anions in the AU. As shown in Figure S6a, both the pyridyl groups in (**7**) merely reside on the same plane and are almost equally twisted in the same direction, forming dihedral angles of 16.0(2) and −18.3(2)° with respect to the central triazole ring. The sulfate salt $H_2L(SO_4)\cdot H_2O$ (**8**) crystallized in the triclinic space group $P\text{-}1$, showing a single ligand, a sulfate anion, and a water molecule in the AU (Figure 3b). In contrast to salt (**7**), one of the pyridyl rings on salt (**8**) is located on the same plane with the central triazole ring, whereas the other pyridyl ring is slightly more tilted from the said plane, as manifested by the dihedral angles of −22.22(19) and 0.97(18)°. Two members of group II resulted from fluorosilicic acid solutions, of which depending on the crystallization conditions, three structurally different salts were obtained. The diprotonated salts H_2LSiF_6 (**9**) and $H_2LSiF_6\cdot 2H_2O$ dihydrated salt (**10**), belonging to group II, crystallized in monoclinic space group $P2_1/c$, whereas one acid solution resulted in a triprotonated hexafluorosilicate salt (**16**) having strongly tilted pyridyl groups (group III). An asymmetric unit of the solvent-free salt (**9**) consists of a single ligand and a $[SiF_6]^{2-}$ anion, and the dihedral angles between the two pyridyl rings and the triazole ring are 26.9(6) and −13.4(5)°. The other hexafluorosilicate salt (**10**) has a $[SiF_6]^{2-}$ anion and two water molecules along with the ligand in an AU and exhibits the highest tilting of the pyridyl rings in group II, dihedral angles being 27.8(2) and 0.4(3)°, respectively. The last salt belonging to group II is $H_2L(HF_2)_2$ (**11**), which crystallizes in a monoclinic $P2_1/c$ space group with an AU comprising one ligand and two $[HF_2]^-$ anions. Analogous to salt (**7**), both the pyridyl groups in (**11**) merely reside on the same plane and are twisted in the same direction, showing dihedral angles of 22.7(2) and −14.9(2)° with relation to the triazole ring.

In group III, triprotonated forms of ligand **L**, H_3L^{3+}, crystallize in the presence of iodide, tetrafluoroborate, perchlorate, and hexafluorosilicate anions, giving rise to H_3LI_3 (**12**), $H_3L(BF_4)_3$ (**13**), $H_3L(ClO_4)_3$ (**14**), $H_3L(ClO_4)_3\cdot 2H_2O$ (**15**), and $H_3L(H_3O)(SiF_6)_2\cdot 2H_2O$ (**16**) salts, respectively (Figure S7). In the case of an iodide solution, salt (**12**) crystallizes in a triclinic space group $P\text{-}1$ with one ligand and three iodide anions in an AU. Explicitly, both the pyridyl groups relative to the central triazole ring are strongly tilted in opposite directions, as indicated by the dihedral angles 31.4(9) and 42.5(9)°. The salt (**13**) crystallizes in monoclinic space group $I2/a$ with one ligand and three tetrafluoroborate anions in an AU. Likewise in (**12**), the tetrafluoroborate salt (**13**) represents strong tilting of pyridyl groups in opposite directions with corresponding dihedral angles of 34.08(18) and 36.92(18)°, thus resulting in also the almost perpendicular orientation of pyridyl rings in relation to each other. The next members of this group were afforded from perchloric acid solutions and presented either an anhydrous form $H_3L(ClO_4)_3$ (**14**) when crystallized in an open vial or hydrate form $H_3L(ClO_4)_3\cdot 2H_2O$ (**15**) when a closed vial was used. Both crystallized in the monoclinic crystal system with $I2/a$ or $P2_1/c$ symmetries, respectively. The AU of salt (**14**) consists of one ligand and three perchlorate anions, resembling the crystal structures of (**12**) and (**13**) by showing dihedral angles of −35.1(2) and −35.8(2)°, respectively (Figure 3c). Contrastingly, perchlorate hydrate salt (**15**) with one ligand, three perchlorate anions, and two water molecules in an AU displays strong tilting of pyridyl rings in the same direction as defined by the dihedral angles 37.7(6) and −36.5(6)°. The last one in group III $H_3L(H_3O)(SiF_6)_2\cdot 2H_2O$ (**16**) crystallizes in a monoclinic $P2_1/c$ symmetry with a single ligand, two hexafluorosilicate anions, one hydronium ion, and two water molecules in its AU. Unlike other members of the group with strongly tilted pyridyl groups, one of the pyridyl rings in the hexafluorosilicate salt (**16**) is leveled with the central triazole ring, and only the second pyridyl ring is strongly tilted as reflected by the dihedral angles 23.9(2) and −3.4(2)°, as shown Table 1.

3.2. Hydrogen Bonding and Molecular Packing. In this work, we have focused on recognizing the interaction of a ligand with anionic species and any water molecules with special emphasis on hydrogen bonding, $\pi-\pi$ stacking, and anion$-\pi$ interactions. We first opted to probe the connections of each of the individual components, namely cationic ligand, anions, and water/hydronium ion, where applicable, in terms of the number of H-bond donor−acceptor units and the nature of interactions. Therefore, the presented H-bonding patterns are categorized based on graph set notations described by Etter et al.[47] From the crystal structures, we were also able to

https://doi.org/10.1021/acs.cgd.3c00393
Cryst. Growth Des. 2023, 23, 5144−5162

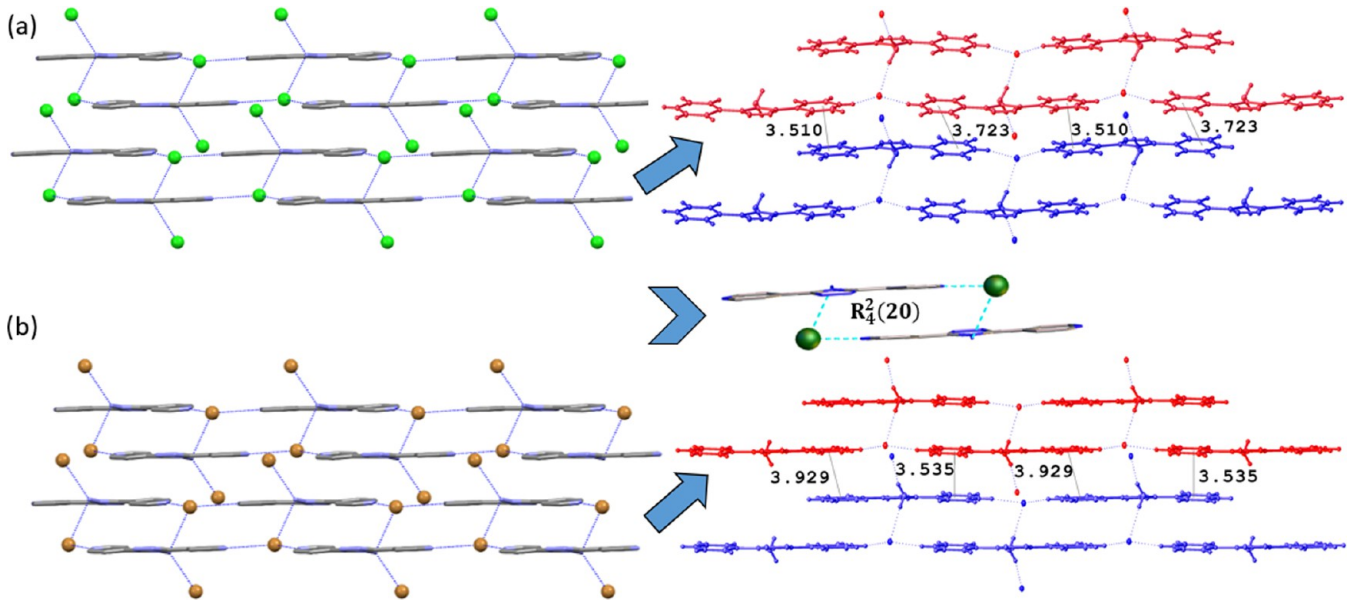

Figure 4. Partial view of molecular packing of the complexes (a) (**1**) and (b) (**2**) along the *b*-axis. The hydrogen-bonded motif present in salt (**1**) is also similar in (**2**). Only relevant atoms are shown. Hydrogen atoms are omitted for clarity. H bonds are exemplified by blue dashed lines (cyan dashed lines in the hydrogen-bonded motif), and the centroid−centroid distances are measured in angstrom (Å).

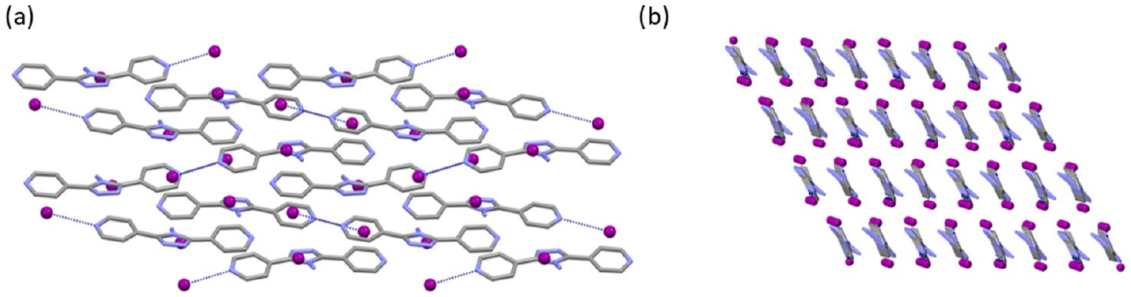

Figure 5. Partial view of molecular packing of salt (**6**) along (a) the *b*-axis and (b) *c*-axis. Hydrogen atoms are omitted for clarity. H bonds are exemplified by blue dashed lines.

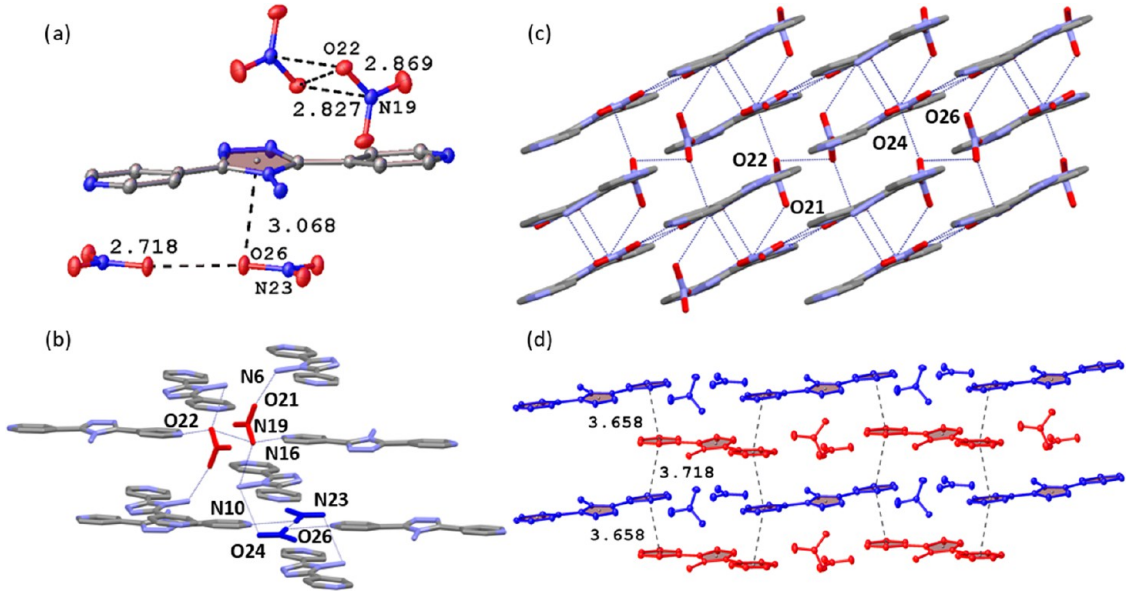

Figure 6. Illustration of salt (**3**) (a) anion−π interactions, (b) schematic representation of nitrate anion hydrogen-bonding connectivity, (c) partial view of molecular packing along the *b*-axis, and (d) stacking interactions: π-stack layer 1 (blue color) and π-stack layer 2 (red color). Only relevant atoms are shown. H bonds are exemplified by blue dashed lines, and the distances are measured in angstrom (Å).

https://doi.org/10.1021/acs.cgd.3c00393
Cryst. Growth Des. 2023, 23, 5144−5162

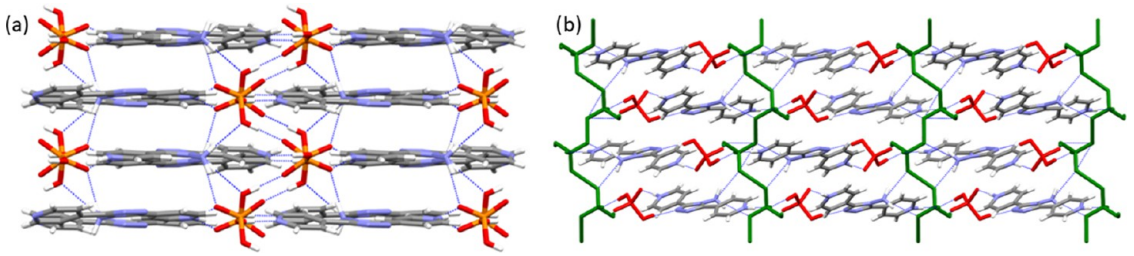

Figure 7. Partial view of molecular packing of the salts (a) (**4**) along the *c*-axis and (b) (**5**) along the *b*-axis. H bonds are exemplified by blue dashed lines.

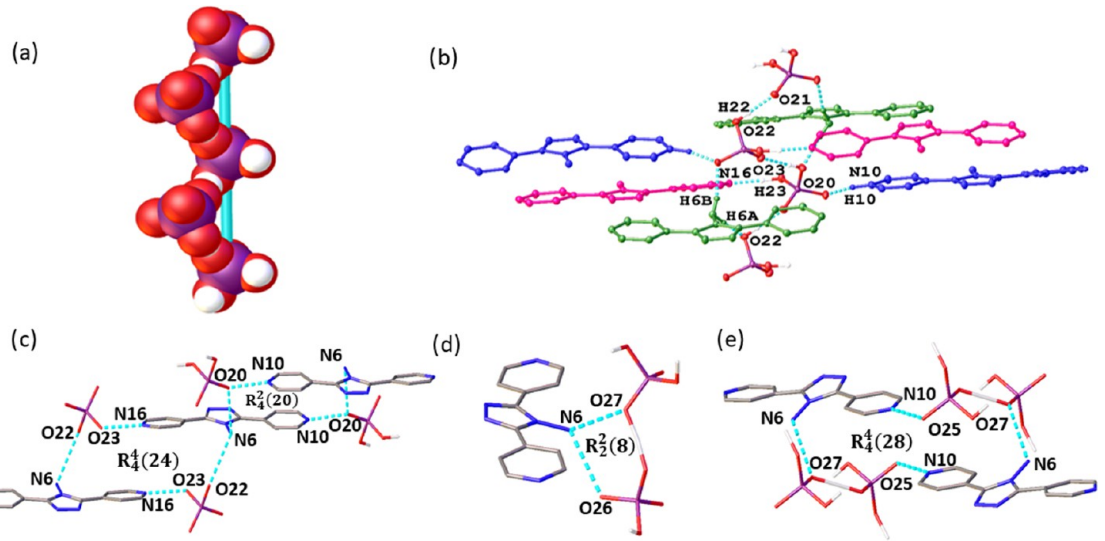

Figure 8. (a) Space-filling representation of hydrogen-bonded dihydrogen phosphate anions forming a helical chain in the salt (**4**) and (b) schematic representation of dihydrogen phosphate anion hydrogen-bonding connectivity. (c) Hydrogen-bonded motifs present in the salt (**4**) and (d, e) in the salt (**5**). H bonds are exemplified by cyan dashed lines. Only relevant atoms are shown.

identify some key structural aspects of anion cluster assembly and anion−water clusters with different counter anions, as presented in following chapters. Hydrogen-bonding geometries for all of the salts are summarized in Table S2. For the sake of simplicity, all of the salts discussed follow the uniform atom labeling of the ligand, as shown in Figure S5a. Additionally, the geometric parameters $d_{centroid}$, d_{plane}, and d_{offset} were applied to define the location of the anion from the triazole ring,[48,49] and are listed in Table S3.

Not surprisingly, salts (**1**) and (**2**) exhibit practically the same packing modes. Both contain H-bonded linear chains of $C_2^1(14)$ (mediated by pyNH$^+$···X interactions) with d(N−X) = ∼3.12 to 3.36 Å, for X = Cl1/Br1 along the *b*-axis. These H bonds further are joined to larger $R_4^2(20)$ H-bonded rings mediated by four molecules (Figure 4). Additionally, (**1**) and (**2**) feature strong face-to-face $\pi-\pi$ interactions in a bricklayer fashion and show centroid−centroid distances of $d(\pi-\pi)$ 3.5105(12)−3.7239(14) and 3.5351(15)−3.9298(15) Å between the pyridyl groups, for (**1**) and (**2**), respectively. Conversely, in the iodide salt (**6**), relatively weak $\pi-\pi$ interactions (face-to-face) between the adjacent pyridyl groups were observed, having centroid−centroid and plane-to-plane shift distances of 3.749(2)−3.824(2) and 1.545(7)−1.886(6) Å, respectively (Figure 5), due to the considerable size difference between anions ($Cl^- < Br^- < I^-$). The diprotonated ligands are packed in antiparallel alignment, resembling columns when viewed along the *c*-axis.

In the salt structure (**3**), anion−π interaction is evident with one of the nitrate anions (designated by N23), which is located 3.2221(8) Å from the centroid of the triazole ring (Figure 6a) with an angle of 9.19(5)° to the plane of the triazole ring. The geometric parameters describing the anion−π interactions are as follows: O26···ring−centroid d(3.0680(11)) Å and O26···ring−plane d(3.0569(11))Å, offset with respect to the normal to the plane is 0.26 Å. The same oxygen atom is involved in strong and almost linear pyNH$^+$···O connections (N−H···O distance, 1.81(2) Å) (Figure 6b). The second oxygen atom (O24) is engaged with amine NH (d(N−O) = ∼3.10 Å), resulting in the formation of infinite zig-zag chains of the ligands with a $C_2^2(12)$ H-bond motif, running parallel to the *c*-axis (Figure 6c). The other nitrate anion (designated by N19) forms an angle of 73.46(5)° to a triazole ring plane, one of its oxygen atoms (O22) bifurcating one short H bond to a pyridinium NH$^+$ and an amine NH, thus forming infinite zig-zag chains of the ligands with $C_2^1(10)$ motifs running parallel to the *b*-axis. The other oxygen atom (O21) shows H bonds with amine NH, of which donor−acceptor distances (N···O) vary from ∼2.7 to 3 Å (Figure 6b). This HB arrangement involving amino groups generates H-bonded chains of the $C_2^2(6)$ motif that runs along the crystallographic *a*-axis. In addition to N−H···O H bonds, oxygen atoms participate in a set of weak but potentially structure-stabilizing aromatic C−H···O interactions (Table S2). The partial view of molecular packing along the crystallographic *a*- and *c*-axis is shown in Figure S8. One of the interesting features of this structure is the origin of $[NO_3]^-$···

https://doi.org/10.1021/acs.cgd.3c00393
Cryst. Growth Des. 2023, 23, 5144−5162

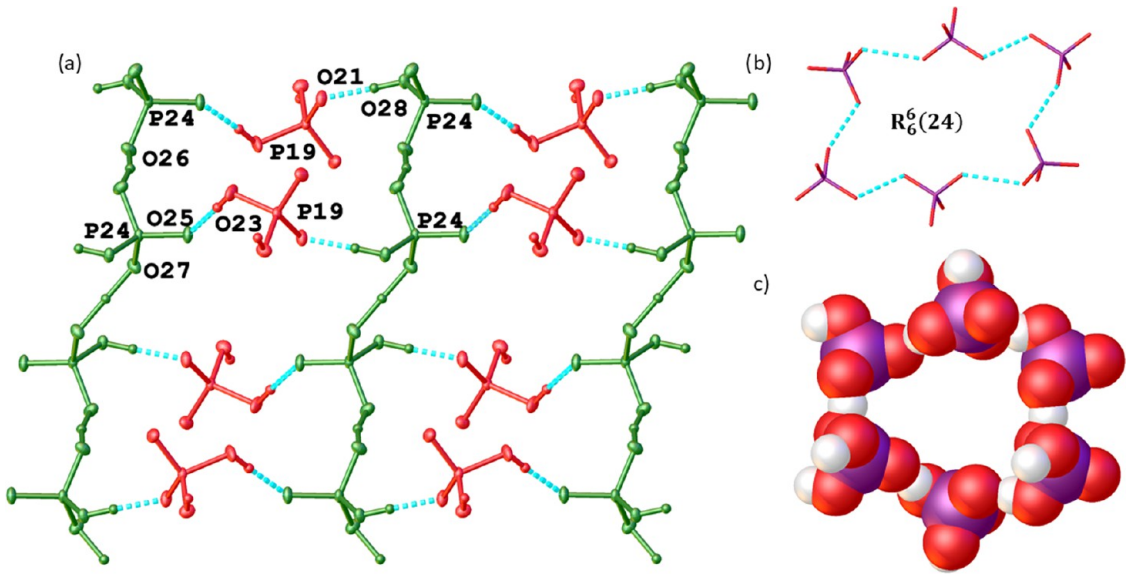

Figure 9. Illustration of the salt (**5**), (a) dihydrogen phosphate anion assembly, (b) hydrogen-bonding motif found in the $(H_2PO_4^-)_6$ aggregate, and (c) space-filling representation of the anion cluster. Cations are omitted for clarity. Only relevant atoms are shown. H bonds are exemplified by cyan dashed lines.

$[NO_3]^-$ interactions. The nitrate anion (N19) is located adjacent to its symmetry twin with an interplanar distance d(N19−N19′) of 3.2905(10) Å. They seem to participate in weak dimer associations, where the central nitrogen atom associates with the oxygen atom of the symmetry-related anion with a short contact of 2.8272(15) Å and d(O22−O22′) being 2.8689(19) Å (Figure 6). Also, the second nitrate anion (N23) is similarly located close by its symmetry twin having two of the oxygen atoms in a face-to-face orientation with a d(O26−O26′) distance of 2.7177(19) Å. The short contacts between these two like-charged ions have been reported also in the literature, e.g., by Kim et al.,[50−53] who suggested that the short contact between two nitrate ions can possibly be caused by packing constraints or supportive attractive interactions further stabilizing the molecular packing. It is worth mentioning that the intriguing work by Mooibroek and coworkers[54] revealed that $[NO_3]^-$ in the solid state could also tend to behave as Lewis π acids, considering that the negative charge of a $[NO_3]^-$ anion is reasonably dampened by interactions, for instance, H bonding or coordination to a metal.[55−57] The packing arrangement of (**3**) exemplifies an intriguing zig-zag π stack: alternately stacking of π-stack layer 1 and π-stack layer 2. As shown in Figure 6d, complex (3) illustrates two kinds of interlayer distances of 3.6584(7) and 3.7185(7) Å.

These results indicate the influence of anion's steric effects on the molecular conformations and the packing. In the salts (**1**) and (**2**), because of the better planarity of ligands and the small size of anions, the interplanar separation between the pyridyl moieties is short, indicating relatively strong $\pi-\pi$ interactions. However, in complex (**3**), nitrate anions exhibit polyhedron conformation, thus forming H bonds with different oxygen atoms and involving other multiple interactions, which stabilize the overall molecular packing. Thus, steric hindrance provided by nitrate anions leads to a modest tilting of pyridyl rings and slightly longer interplanar separation between the pyridyl moieties, indicating relatively weak $\pi-\pi$ stacking.[58]

Salts (**4**) and (**5**) form layered structures composed of chains or H-bond-directed cluster assemblies of dihydrogen phosphate anions (Figure 7). The monoprotonated salt (**4**) also comprises a layered structure of anions and cations like complex (**5**) but with a distinct H-bonding arrangement. The change is reflected in the formation of an infinite helical chain around a 2_1-screw axis sustained by O−H···O H-bonds with d(O22−O21) being 2.5417(18) Å and propagating along the b-axis (Figure 8a). The helical chains are further connected across by the monoprotonated ligand, in a "stair-steps" manner (Figure 8b). Thus, two hydrogen atoms from amino groups, in a *syn* manner, connect the two oxygen atoms (O20 and O22) of $[H_2P(19)O_4]^-$ to form an infinite $C_2^2(6)$ type H-bonded chain that runs parallel to the b-axis and being orthogonal to the H-bonded chain of $C_2^2(16)$ type (mediated via O23−H23···N16 and N10−H10···O20). As a result of the intersection of these chains, the H-bonded ring patterns $R_4^2(20)$ and $R_4^4(24)$ are generated in the structure (Figure 8c). The partial view of the molecular packing along the c-axis is shown in Figure 7a. The complex (**5**) contains two crystallographic distinct dihydrogen phosphate anions $[H_2P(24)O_4]^-$ and $[H_2P(19)O_4]^-$, with $[H_2P(24)O_4]^-$ possessing a disordered hydrogen atom over two positions (H26 and H27) with 0.5 occupancies each. Both dihydrogen phosphate anions exhibit different coordination environments. Anion $[H_2P(24)O_4]^-$ develops an infinite zig-zag chain involving two sets of O−H···O hydrogen bonds (O···O = ∼2.5 Å) that run parallel to the a-axis. Most interestingly, two equivalent zig-zag chains are interlinked by a second phosphate anion via a strong O−H···O H bonds with the $R_6^6(24)$ motif forming a hexameric cluster $(H_2PO_4^-)_6$, which consists of alternating two P(24) and P(19) anions that propagate into a H-bond-directed anion cluster assembly when viewed down the c-axis, as shown in Figure 9. In this $R_6^6(24)$ motif generated, the dihydrogen phosphate anion P(19) is involved in a total of four H bonds with neighboring chains by acting both as an acceptor (O21) and a donor (O23−H23), respectively. Thus, the hexameric cluster identified resembles a cyclohexane-like structure,[17] wherein four dihydrogen phosphate anions (P24) of the cyclic ring reside on the same plane and two other anions (P19) lie above and below the plane. The anion cluster assembly formed is not flat, but it displays kind of a corrugated pattern. The

https://doi.org/10.1021/acs.cgd.3c00393
Cryst. Growth Des. 2023, 23, 5144−5162

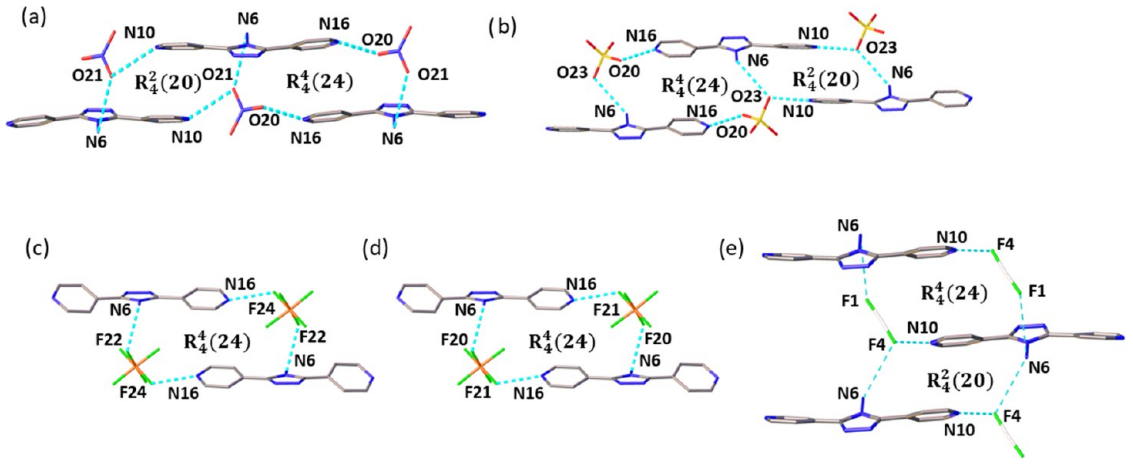

Figure 10. Hydrogen-bonded motifs present in the salts of group II. (a) In salt (**7**), (b) salt (**8**), (c) salt (**9**), (d) salt (**10**), and (e) salt (**11**). Only relevant atoms are shown. Hydrogen atoms are omitted for clarity. H bonds are exemplified by cyan dashed lines.

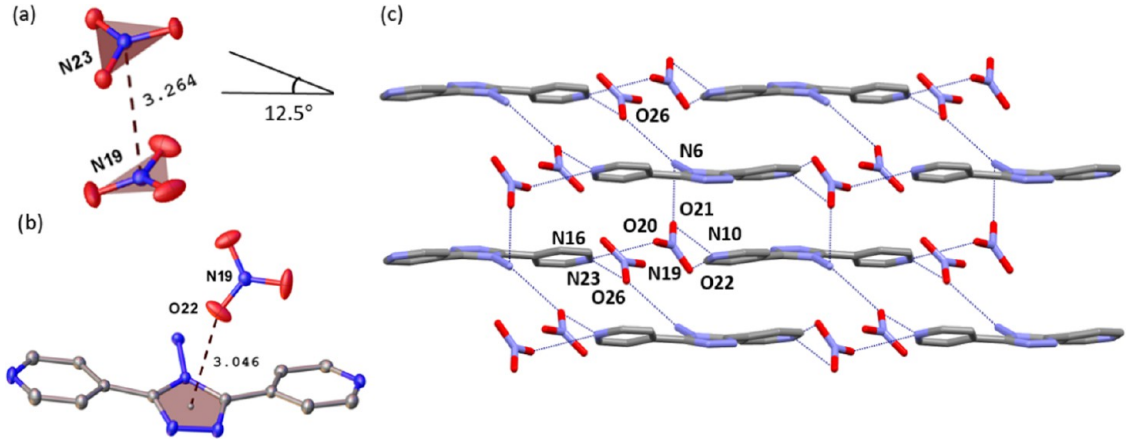

Figure 11. (a) Canted anion pairs in the salt (**7**), (b) anion−π interactions, and (c) partial view of molecular packing along the *b*-axis. Hydrogen atoms are omitted for clarity. H bonds are exemplified by blue dashed lines. Only relevant atoms are shown, and the distances are measured in angstrom (Å).

observed intermolecular O···O contact distances in this anionic hexamer cluster range between 2.51 and 2.63 Å and are similar to one observed by Hoque et al. and Mahé et al.[17,59,17,59] Further, the dihydrogen phosphate anion $[H_2P(19)O_4]^-$ interacts with two cationic ligands through a triazole ring nitrogen acceptor (N4) and to a pyridinium NH^+ donor (N16−H16) with infinite $C_2^2(11)$ H-bonded motif chains running parallel to the *b*-axis, while the other $[H_2P(24)O_4]^-$ form contacts with a ligand via amino (N6−H6a and N6−H6b) and $pyNH^+$ donors (N10−H10) forming $R_2^2(8)$ and $R_4^4(28)$ geometry types (Figure 8d,e). The partial view of molecular packing along the *b*-axis is shown in Figure 7b.

The molecular packing arrangements of the group II salts (**7**−**11**) exhibit also layered H-bonded networks comprising anions and cationic ligands. Salts (**8**) and (**10**) of the group are slightly different from the others as they also contain water molecules and by that represent a somewhat wider range of H-bonding motifs. Interestingly, two types of H-bonded cyclic ring motifs were observed, namely, $R_4^2(20)$ and/or $R_4^4(24)$ (Figure 10) as structural units governed by the conformation of the bent ligand and the type of the anion.

Differing from the previously considered salt (**3**), in the triclinic nitrate salt (**7**), the nitrate anions do not participate in any dimer associations. The nitrate anion (N19) is located 4.2263(11) Å from the centroid of the triazole core with an angle of 125.31(7)° to a triazole ring plane, while another nitrate anion (N23) is 5.5793(12) Å apart with an angle of 42.41(6)° to the said plane. The nitrate anions occur in pairs with an interplanar distance of 3.2642(10) Å and are canted by 12.5° relative to each other (Figure 11a). The hydrogen bonding of salt (**7**) is also significantly different compared to salt (**3**). Both $pyNH^+$ donors are engaged in bifurcated H-bonding, wherein one protonated pyridyl (N10) bifurcates two oxygen atoms (O21 and O22) of one anion to form the $R_1^2(4)$ structural motif, whereas the other protonated pyridyl (N16) bifurcates two oxygen atoms (O20 and O26) of two anions, overall facilitating the formation of infinite linear H-bonded chains of $C_2^2(16)$ type, running parallel to the *c*-axis (Figure 11c). The hydrogen atoms of the 6-NH_2 groups act as H-bond donors to the oxygen atom (O21) of one nitrate anion (N19) and the oxygen atom (O26) of a second nitrate anion (N23) and unite these chains into layers via N−H···O H bonds (d(N···O) = ∼2.8 to 3.0 Å), forming a combination of two H-bonded ring patterns of $R_4^2(20)$ and $R_4^4(24)$ types (Figure 10a). The intermolecular H bonds are further stabilized by weak C−H···O interactions, π−π stacking interactions between the adjacent pyridyl groups (N10) with a centroid−centroid distance $d(\pi-\pi)$ of 3.7574(7) Å, and anion−π interactions

https://doi.org/10.1021/acs.cgd.3c00393
Cryst. Growth Des. 2023, 23, 5144−5162

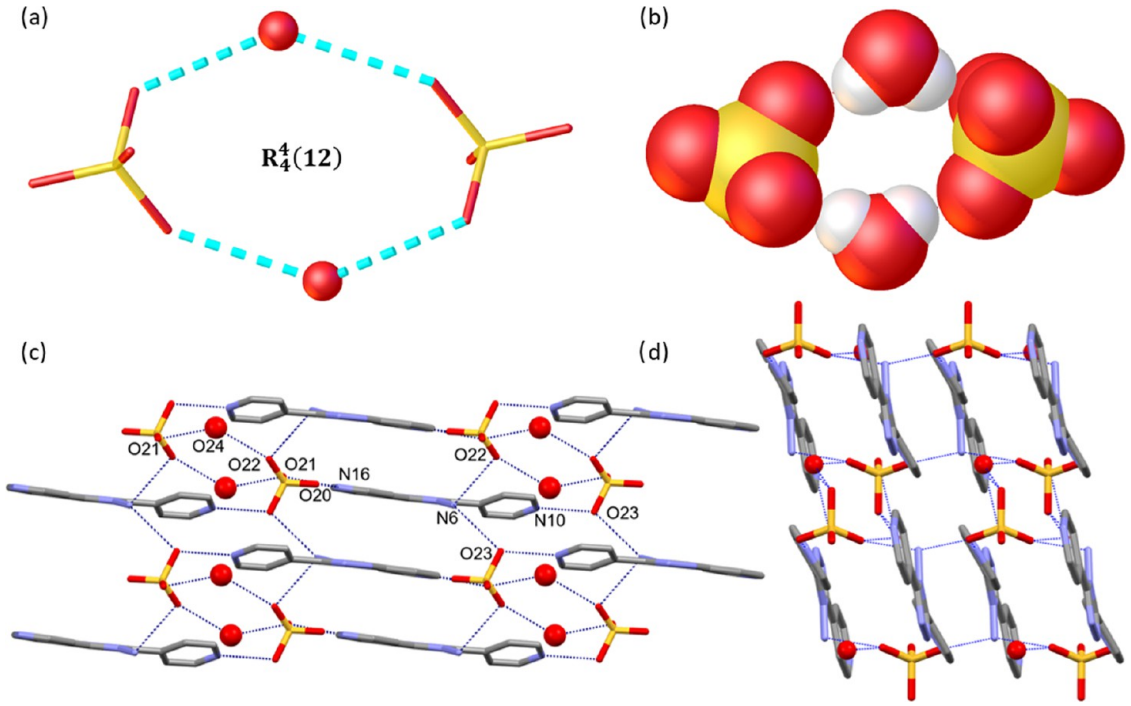

Figure 12. (a) Hydrogen-bonding motif found in the sulfate−water cluster in the salt (**8**), (b) space-filling representation of the sulfate−water tetramer, and partial view of molecular packing along the (c) *b*-axis and (d) *c*-axis. Hydrogen atoms are omitted for clarity. H bonds are exemplified by blue dashed lines (cyan dashed lines in the sulfate−water cluster). Only relevant atoms are shown.

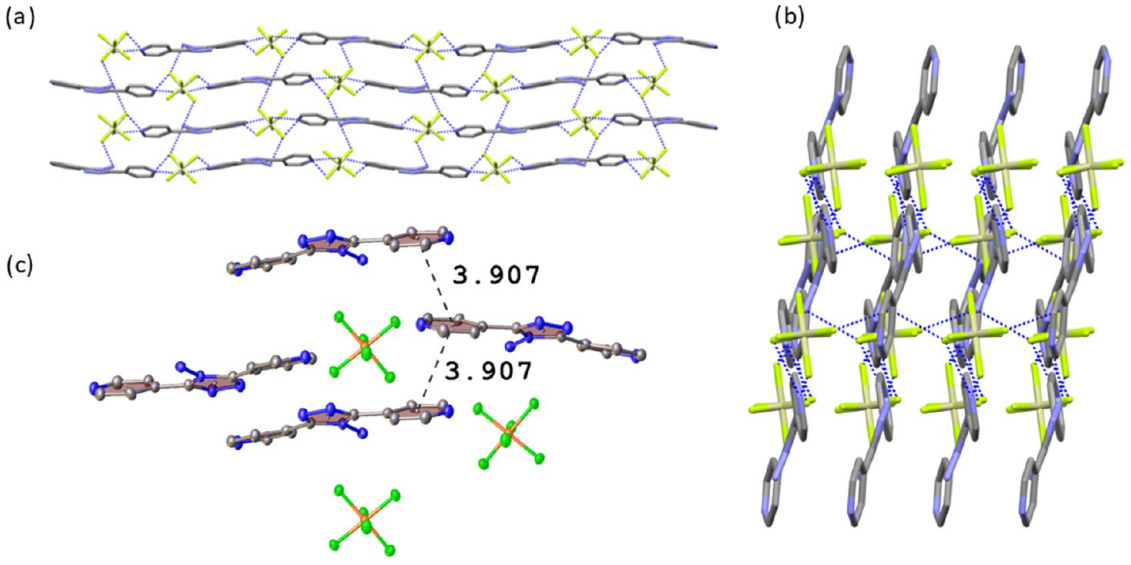

Figure 13. Partial view of molecular packing of the salt (**9**) (a) along the *a*-axis, (b) along the *b*-axis, and (c) stacking interactions. Only relevant atoms are shown. H bonds are exemplified by blue dashed lines, and the centroid−centroid distances are measured in angstrom (Å).

d(O22−centroid\offset distances of 3.0455(16)/1.26 Å), as shown in Figure 11b. The molecules are assembled in layers parallel to the *ac*-plane, as shown in Figure 11c.

The most appealing feature of (**8**) is the presence of an anion−water cluster.[17] The single water molecule (O24) is H-bonded with two neighboring sulfate anions [O24···O22 = 2.7955(17) Å and O24···O21 = 2.7921(17) Å] to give a cyclic tetramer $[(SO_4)_2{-}(H_2O)_2]^{4-}$ cluster of $R_4^4(12)$ geometry type, located around the inversion center (Figure 12). Noticeably, the small sulfate−water cluster does not engage in any interactions between themselves but instead forms contacts with pyridinium NH^+ and 6-NH_2 groups. As shown in Figure 12c, one hydrogen atom of the protonated pyridyl (N16) bifurcates two oxygen atoms of a sulfate anion (O21 and O20) to construct the $R_1^2(4)$ structural motif and the other, pyridinium (N10) forms a single bond with sulfate oxygen (O23). The N−H^+···O bonds link the cationic ligands and anions into infinite chains of $C_2^2(16)$ type parallel to the *c*-axis with N···O distances of about 2.65−2.98 Å. The 6-NH_2 groups are engaged in a $C_2^2(6)$ chain which propagates along the *a*-axis orthogonal to the $C_2^2(16)$ H-bonded chain. As a result, the combination of HB geometries generates $R_4^2(20)$ and $R_4^4(24)$ types of H-bonded rings mediated by four molecules, as shown in Figure 10b. The molecular packing along the *b*-axis displays

https://doi.org/10.1021/acs.cgd.3c00393
Cryst. Growth Des. 2023, 23, 5144−5162

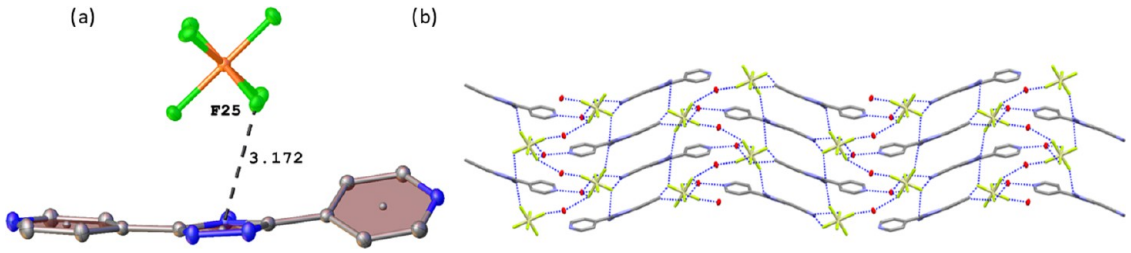

Figure 14. (a) Anion−π interactions and (b) partial view of molecular packing along the *a*-axis in salt (**10**). Only relevant atoms are shown. H bonds are exemplified by cyan dashed lines, and the distance is measured in angstrom (Å).

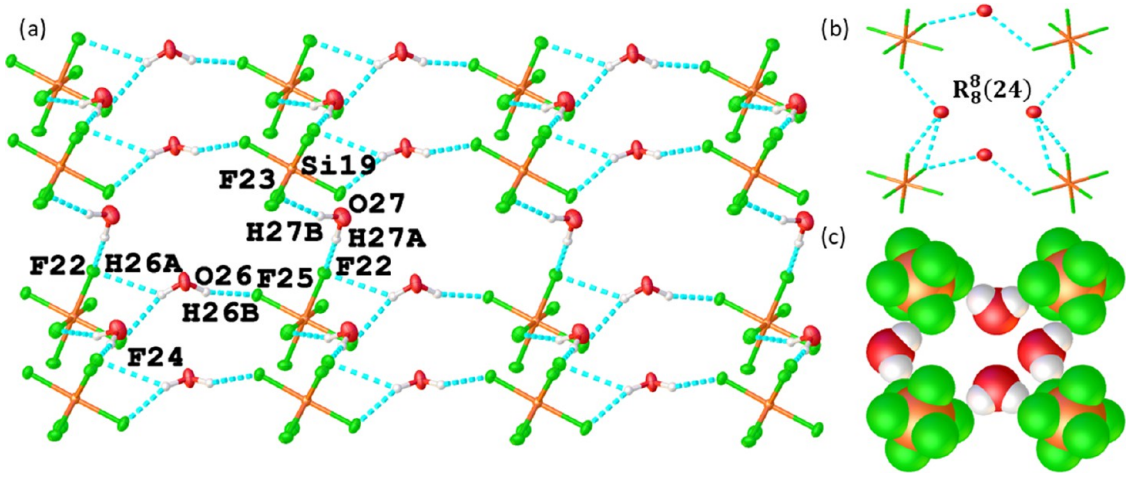

Figure 15. Illustrations of the salt (**10**). (a) Anion−water assembly, (b) hydrogen-bonding motif found in the cyclic octameric cluster, and (c) space-filling representation of the anion−water cluster. Cations are omitted for clarity. Only relevant atoms are shown. H bonds are exemplified by cyan dashed lines.

a layered array of cationic ligands with the inclusion of a sulfate−water cluster inserted in the space between H_2L^{2+}, as shown in Figure 12.

The hexafluorosilicate salts displayed a diverse range of structural features. Two of the hexafluorosilicate structures (**10**) and (**16**) comprise water in their lattice, while (**9**) is anhydrous. As shown in Figure 13, salt (**9**) exhibits wave-like layers of ions when viewed along the *a*-axis. The 6-NH_2 groups are engaged in N−H···F interactions, forming H-bonded chains of $C_2^2(6)$ type parallel to the *c*-axis, whereas wave-like H-bonded chains of $C_2^2(16)$ type (mediated by protonated pyridyl rings and fluorine atoms) go along the *b*-axis. There is also $R_4^4(24)$ H-bonded geometry type analogous to those observed for other members of this group (Figure 10c). Moreover, the packing is facilitated by C−H···F contacts and weak face-to-face $\pi\cdots\pi$ stacking with the pyridyl groups' centroid−centroid distance being $d(\pi-\pi)$ 3.9079(11) Å (Figure 13).

Contrary to (**9**), in the salt (**10**), the layered array of cationic ligands and fluorosilicate anion exists, as alternating anion−water sheets, to generate a wave-like layered structure when viewed along the *a*-axis (Figure 14). The H-bond environment around the hexafluorosilicate unit is intriguing, where each $[SiF_6]^{2-}$ anion accepts eight hydrogen bonds, out of which, 6-NH_2 groups and pyridinium NH^+ of cationic ligands contribute to three N−H···F interactions and water molecules via five O−H···F H-bond interactions. The water molecule (O26) also acts as a H-bond acceptor toward the pyridinium (N10) group via a single N−H···O H-bond, while as H donors they connect two $[SiF_6]^{2-}$ anions, with one bifurcating hydrogen (H26) and one with a single contact (H26B) to form infinite chains of $C_2^2(6)$, running parallel to the *a*-axis. Two identical chains are further strongly stitched via a second water molecule (O27) via two O27−H27A···F22 and O27−H27b···F23 H-bonds, forming cyclic octameric clusters $[(SiF_6)_4-(H_2O)_4]_\infty^{8-}$ with a structural motif $R_8^8(24)$ that results in undulated sheet propagating along the *a*-axis (Figure 15a).[60,61] Further, each cationic ligand bridges the anion−water cluster assembly via N−H···O and N−H···F H bonds, resulting in structural motifs $R_4^4(24)$ with D···A distances of about 2.6−3.0 Å (Figure 10d). Apart from N−H···O, O−H···F, and N−H···F H-bond interactions, the hydrogen bonding-driven assembly is further stabilized by anion−π interactions *d*(F25−centroid\offset distances of 3.1717(12)/1.35 Å), as shown in Figure 14a.

Ions in the salt (**11**) pack as layered sheets held by a network of N−H···F and C−H···F interactions, as shown in Figure S9. The F2 atom of $[H(2)F_2]^-$ ions is linked with pyridine NH^+ units that assemble into linear H-bonded chains of $C_2^1(14)$ running parallel to the *a*-axis. These chains are further linked in the second direction via C9−H9···F3 interactions (Table S2). Further, H bonds involving 6-NH_2 groups are centered on F1 and F4 atoms of the second $[H(2)F_2]^-$ ion facilitating H-bonded chains of $C_2^2(6)$ type running parallel to the *b*-axis. The F4 atom also forms contacts via N10−H10···F4 and C15−H15···F4 interactions in alternating layers. As a result, analogous to previous structures, the crystal structure of (**11**) is also built by the combination of $R_4^2(20)$ and $R_4^4(24)$ H-bonded ring patterns (Figure 10e).

The iodide salt (**12**) in group III differs completely from the iodide structure (**6**) belonging to group I, as it exhibits

https://doi.org/10.1021/acs.cgd.3c00393
Cryst. Growth Des. 2023, 23, 5144−5162

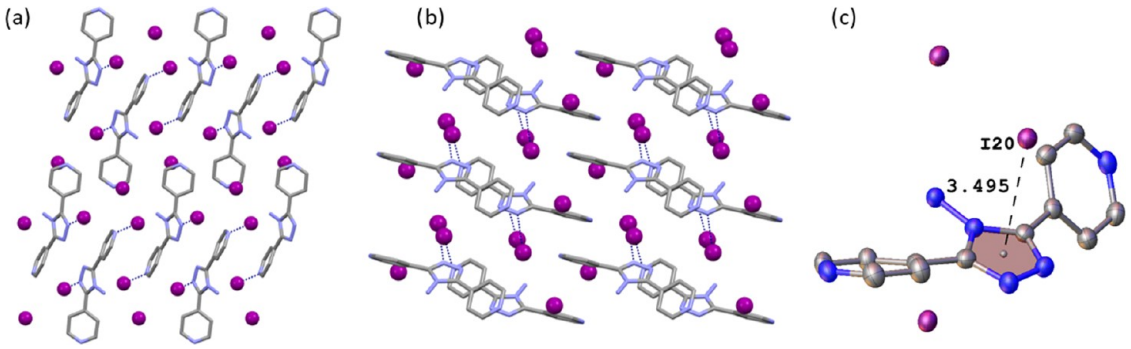

Figure 16. Partial view of molecular packing of (**12**) (a) along the *a*-axis, (b) along the *b*-axis, and (c) anion−π interactions. Hydrogen atoms are omitted for clarity. Only relevant atoms are shown. H bonds are exemplified by blue dashed lines, and the distance is measured in angstrom (Å).

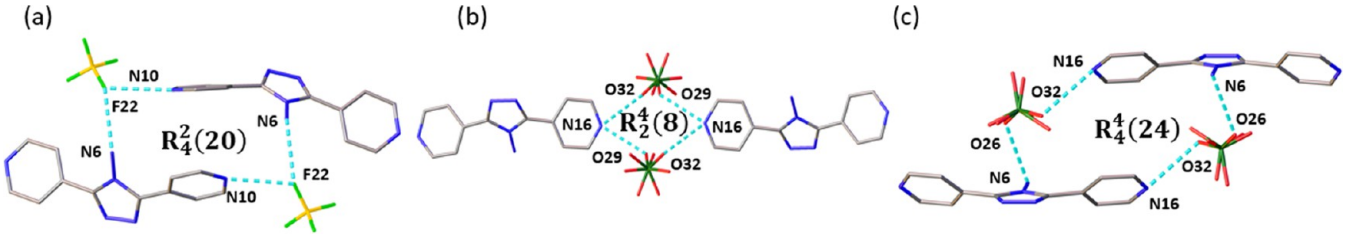

Figure 17. Hydrogen-bonding motifs present in the salts of group III. (a) In salt (**13**) and (b) and (c) in salt (**15**). Only relevant atoms are shown. Hydrogen atoms are omitted for clarity. H bonds are exemplified by cyan dashed lines.

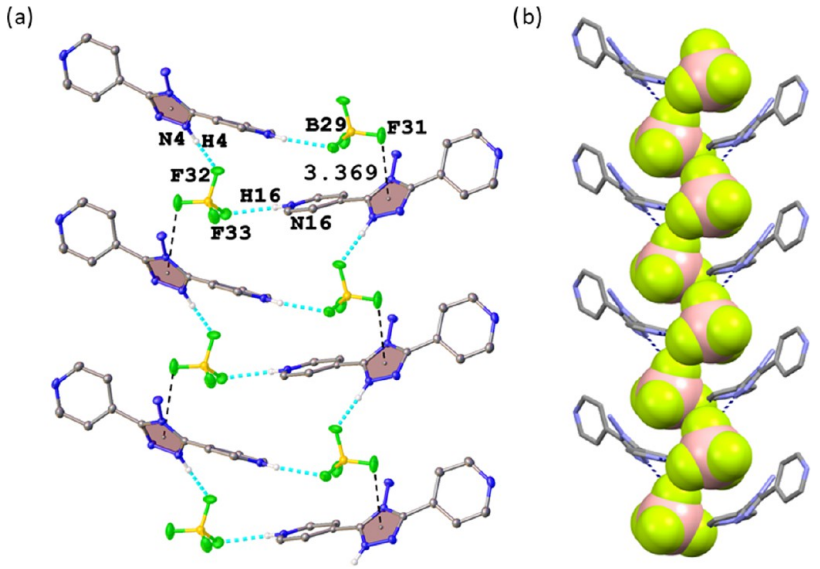

Figure 18. Illustrations of salt (**13**) (a) anion−π interactions and (b) hydrogen-bonded 1D chain along the *c*-axis. Only relevant atoms are shown. H bonds are exemplified by cyan dashed lines.

anion−π interaction with the following features: I20···ring−centroid distance *d*(3.495(2)) Å and I20···ring−plane distance *d*(3.456(3)) Å with the offset of 0.52 Å to the normal of the plane. The same anion (I20) is also involved in a weak N10−H10···I20 H-bond interaction with a distance *d*(N−I) of 3.506(7) Å. The partial view of molecular packing displaying anion−π interactions along the *a*- and *b*-axes is shown in Figure 16.

The structure of salt (**13**) reveals a layered arrangement stabilized by mainly N−H···F H-bonds (Figure 17) and anion−π interactions, as shown in Figure S10. In total, three tetrafluoroborate anions accept seven H bond interactions with N···F distances varying from ∼2.7 to 3 Å. One tetrafluoroborate anion $[B(29)F_4]^-$ involves two different fluoride atoms to link two cationic ligands via N4−H4···F32 and N16−H16···F33 H bonds in a continuous fashion, forming 1D chains ($C_2^2(11)$) related by the 2_1-screw axis (Figure 18) that develops along the *b*-axis. In this H-bonded 1D chain, one of the fluorine atoms (F31) being only 3.3691(14) Å apart from the triazole ring centroid appears to engage in anion−π interactions (Figure 18). These 1D H-bonded chains are then assembled into a 2D layered arrangement along the *b*-axis by another $[B(19)F_4]^-$ anion that serves as a bridge to link these adjacent chains via N10−H10···F22 and N6−H6A···F22 (Figure 19), resulting in the $R_4^2(20)$ H-bonded structural motif (Figure 17a). The third tetrafluoroborate $[B(24)F_4]^-$

https://doi.org/10.1021/acs.cgd.3c00393
Cryst. Growth Des. 2023, 23, 5144−5162

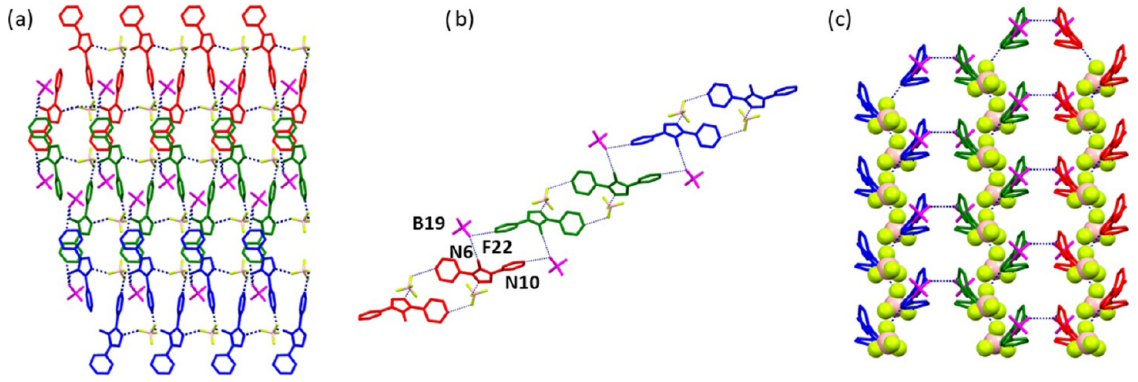

Figure 19. Partial view of the 2D layer of (**13**) (a) along the *a*-axis, (b) along the *b*-axis, and (c) along the *c*-axis. Hydrogen atoms are omitted for clarity. Only relevant atoms are shown. H bonds are exemplified by blue dashed lines.

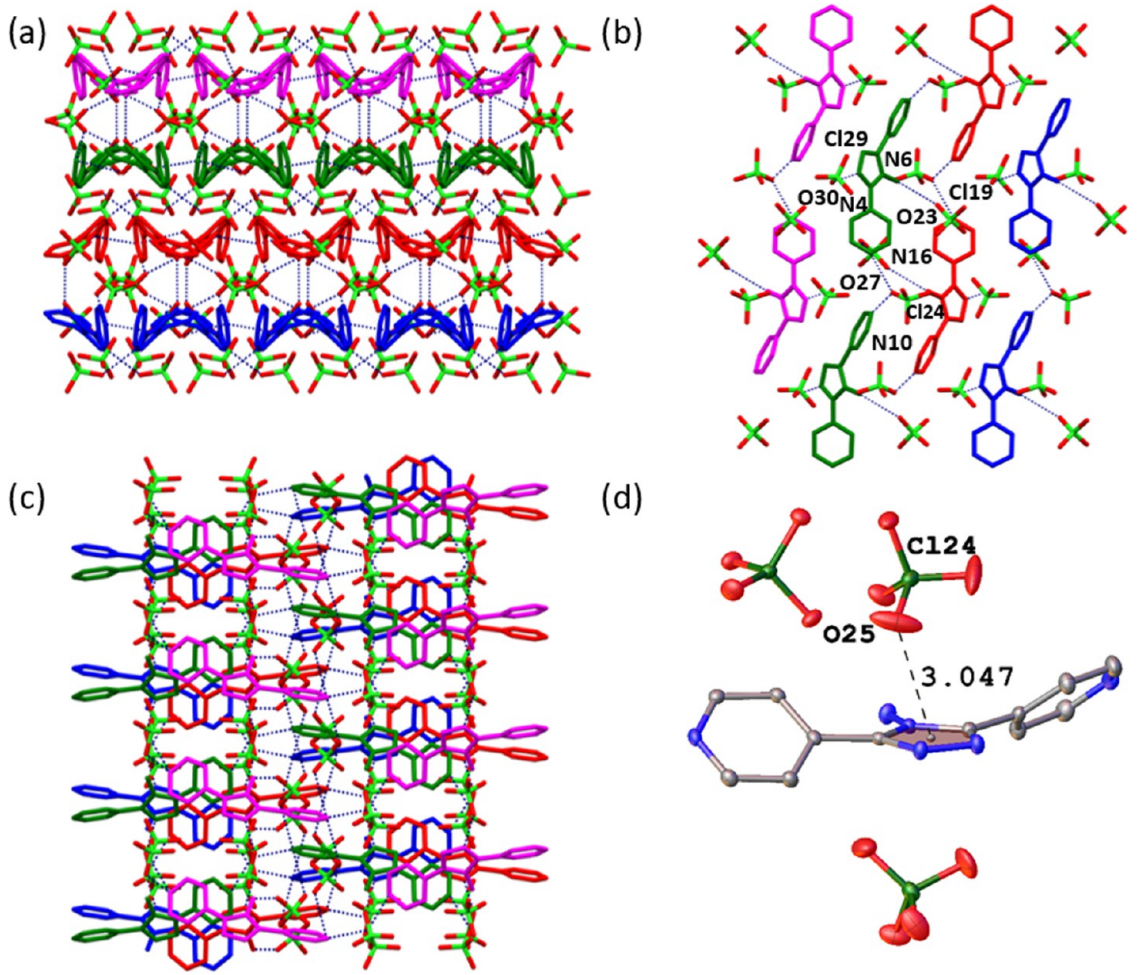

Figure 20. Partial views of molecular packing of (**14**) (a) along the *a*-axis, (b) along the *b*-axis, (c) along the *c*-axis, and (d) anion−π interactions. Hydrogen atoms are omitted for clarity. H bonds are exemplified by blue dashed lines, and the distance is measured in angstrom (Å).

anion engages in three N−H···F H-bond interactions, where the fluoride atom (F26) behaves as a bifurcated H-bond acceptor involving protonated pyridyl (N10−H10···F26 and N16−H16···F26) to form a helical chain of the $C_2^1(14)$ structural motif, which propagates parallel to the *c*-axis (Figure S10). The further link of the fluoride atom (F25) of the $[B(24)F_4]^-$ anion with an amino group (N6−H6A···F25) facilitates the formation of a double chain arrangement ($C_2^2(12)$) along the *b*-axis, as shown in Figure S10.

In the perchlorate salt (**14**), the ligand is triprotonated with three perchlorate anions of which molecular packings are shown in Figure 20 along *a*-, *b*-, and *c*-axes. The $[Cl(24)O_4]^-$ oxygen atom (O27) is engaged in two H bonds with two protonated ligands forming an infinite zig-zag H-bonded chain of the $C_2^1(14)$ motif, propagating along the *a*-axis. Both the triazole (N4) and amino (N6) are connected to the other two perchlorate anions $Cl(29)O_4^-$ and $Cl(19)O_4^-$ via N−H···O H bonds, respectively. Interestingly, there are also anion−anion interactions between the perchlorate anions with distances of

https://doi.org/10.1021/acs.cgd.3c00393
Cryst. Growth Des. 2023, 23, 5144−5162

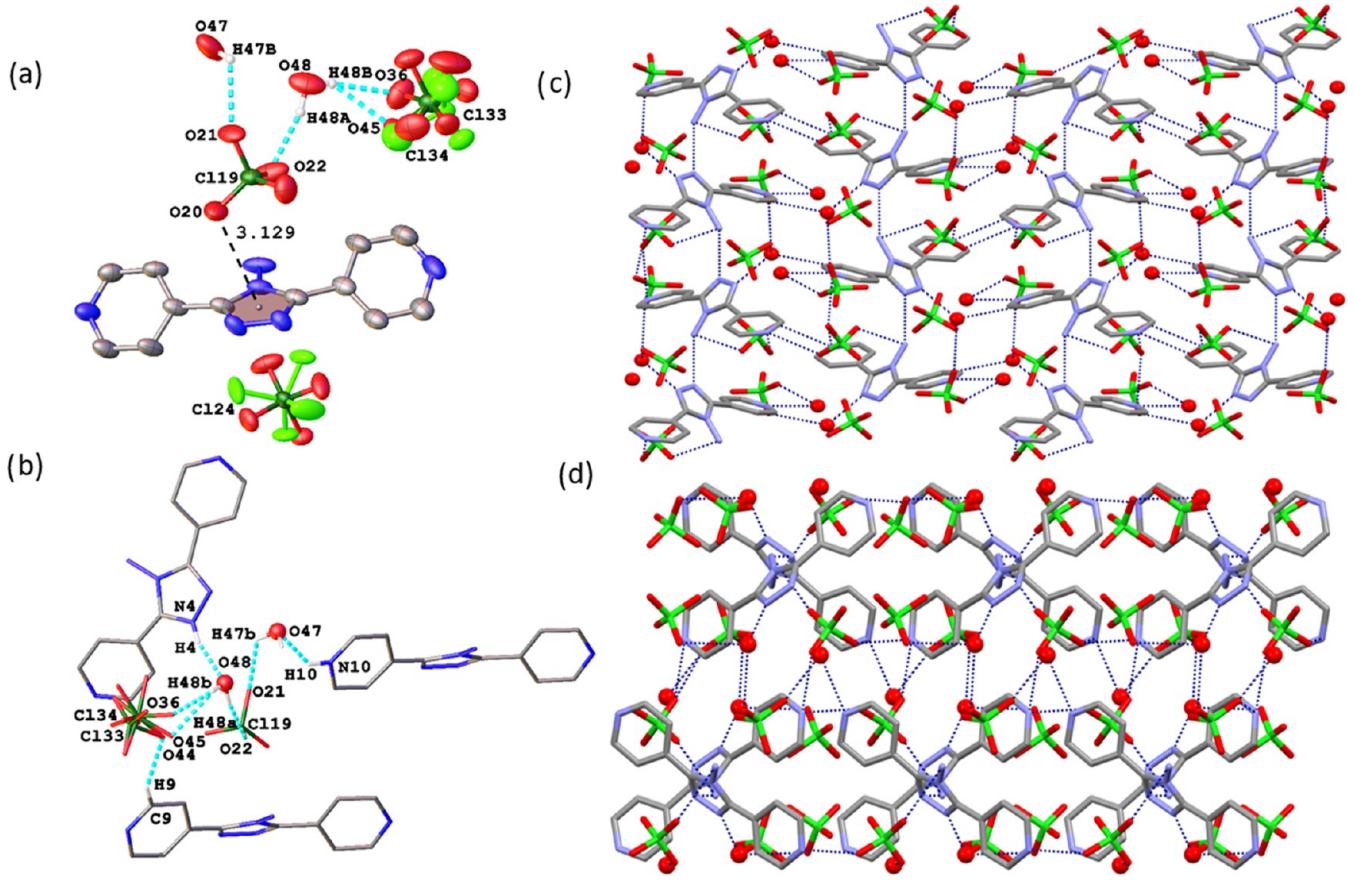

Figure 21. Illustration of (**15**) (a) acyclic $(ClO_4^-)_2(H_2O)_2$ tetramer and anion−π interactions, (b) coordination environment around the acyclic $(ClO_4^-)_2(H_2O)_2$ tetramer, and (c) molecular packing along the *a*-axis and (d) along the *c*-axis. Only relevant atoms are shown. Hydrogen atoms are omitted for clarity. H bonds are exemplified by cyan dashed lines (blue dashed lines in molecular packing), and the distance is measured in angstrom (Å).

3.006(2), 2.9631(19), and 3.040(2) Å for *d*(O33−O22), *d*(O23−O27), and *d*(O27−O33), respectively.[61] Notably, the oxygen atom (O25) of $[Cl(24)O_4]^-$ is also in close proximity to the triazole ring centroid with an O25···ring−centroid distance of *d*(3.0468(17)) Å and an O25···ring−plane distance of *d*(2.845(2)) Å with an offset distance of 1.09 Å, indicating anion−π interaction (Figure 20d).

Considerably different structural features are observed for the salt (**15**) containing water molecules, which seems to participate in the formation of an acyclic $(ClO_4^-)_2(H_2O)_2$ tetramer moiety (Figure 21a). One of the $[ClO_4]^-$ anions is disordered with approximate occupancies of 0.8 and 0.2, respectively, for Cl34 and Cl33, and the four oxygen atoms for the same anion are disordered over three positions with approximate occupancies of 0.4:0.4:0.2. Similarly, in case of the second $[Cl(24)O_4]^-$ anion, its oxygen atoms are disordered over two positions with approximate occupancies of 0.6 and 0.4. In contrast to another perchlorate salt (**14**), the number of H bonds varies significantly due to the presence of water molecules. In total, three cationic ligands surround the acyclic cluster via N−H···O and C−H···O H-bond interactions (Figure 21b). In this perchlorate−water−perchlorate−water cluster, there are two crystallographically distinct perchlorate ions and two crystallographically distinct water molecules (O48 and O47). The $[Cl(19)O_4]^-$ anion is not H-bonded to the protonated ligand but instead has two water O−H···O intracluster H bonds (O47−H47B···O21 and O48−H48A···O22). Both water molecules are then H-bonded to the cationic ligand (Figure 21b). The oxygen (O47) of a water molecule is engaged with pyridinium N10−H10B···O47, whereas the second water molecule (O48) is coordinated through a strong N4−H4···O48 H bond, forming zig-zag chains parallel to the *b*-axis (Figure 21c). The coordination environment of the third perchlorate ion $[Cl(24)O_4]^-$ is entirely different, as it only bounds to the protonated ligand and has no contact with nearby water molecules (Figure 21c). Each $[Cl(24)O_4]^-$ participates in three N−H···O bonds by three cationic ligands. The perchlorate oxygen atoms O29 and O32 (0.6 occupancy each) are in contact with pyridine hydrogen donor N16−H16, forming a centrosymmetric $R_2^4(8)$ H-bonded ring motif (Figure 17b). The amino group hydrogen (N6−H6B) is shared by the third oxygen atom O26 of $[Cl(24)O_4]^-$, facilitating the formation of H-bonded chains $C_2^2(12)$, propagating along the *a*-axis and being part of the $R_4^4(24)$ H-bonding motif (Figure 17c). Interestingly, the direct interactions between two cationic ligands are also observed. This mediates via an amino donor (N6−H6B) and a triazole nitrogen acceptor (N3) with a contact distance *d*(N6−N3) of 2.981(5) Å, and also facilitates the formation of $C_1^1(5)$ H-bonded chains propagating along the *c*-axis (Figure 21c). The molecular packing when viewed along the *c*-axis shows the criss-cross orientation of cationic ligands (Figure 21d). Besides the multisite (N−H···O, C−H···O and O−H···O) H-bond interactions around the anions, the molecular packing is further stabilized by anion−π contacts.

https://doi.org/10.1021/acs.cgd.3c00393
Cryst. Growth Des. 2023, 23, 5144−5162

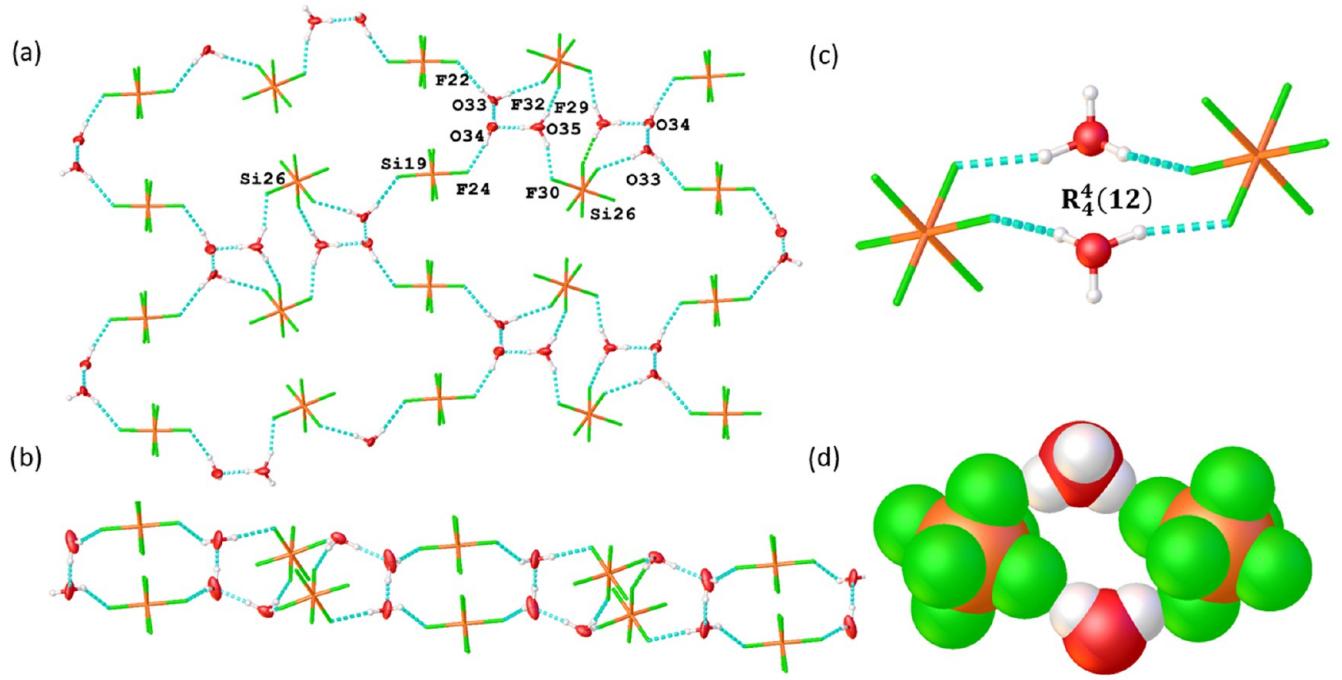

Figure 22. Illustrations of (**16**) (a) hydrogen-bonded sheet of water molecules, hexafluorosilicate anions and hydronium ions, (b) side view of the same sheet, (c) hydrogen-bonding motif found in the cyclic tetrameric cluster, and (d) space-filling representation of the cyclic tetrameric cluster. Cations are omitted for clarity. Only relevant atoms are shown. H bonds are exemplified by cyan dashed lines.

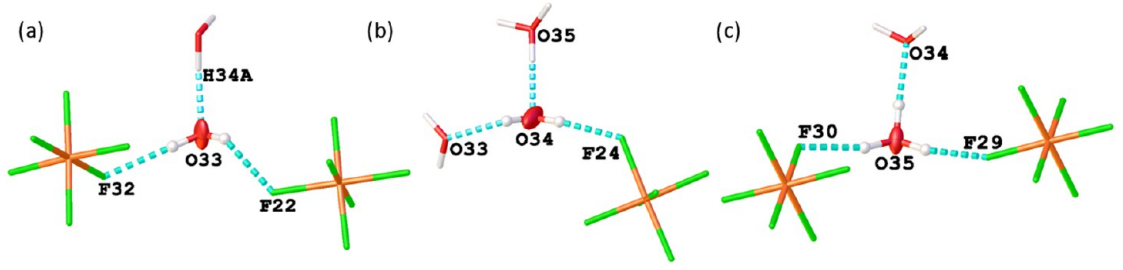

Figure 23. Hydrogen-bonding environment of different water molecules and the hydronium ion in the structure (**16**). Only relevant atoms are shown. H bonds are exemplified by cyan dashed lines.

The perchlorate anion $[Cl(19)O_4]^-$ contributes to anion−π interactions, as one of its oxygen atoms (O20, with no disorder) is at close proximity from the triazole ring with a distance d(O20−centroid) of 3.129(4) Å and an offset of 1.19 Å to the centroid (Figure 21a).

Different from the other hexafluorosilicate structures, the ligand in the salt (**16**) is triprotonated, and the salt contains water along with the anions of which also a hydronium ion was found to balance the overall charge due to two hexafluorosilicate anions. In this structure, infinite H-bonded sheets comprised of water molecules, hexafluorosilicate anions, and hydronium ions can be observed. The sheet-like arrangement features several cyclic motifs, namely, tetrameric and 16-membered cyclic motifs, all interconnected, as shown in Figure 22. In the cyclic tetramer ring, a hydronium ion (O35) serves as a H-bond donor toward F29 and F30 of $[Si(26)F_6]^{2-}$, giving a centrosymmetric $R_4^4(12)$ H-bonded structural motif that eventually brings together two hydronium units and two $[Si(26)F_6]^{2-}$ anions. Thus, the hydronium ion (O35) is situated between two $Si(26)F_6^{2-}$ anions and one water molecule (O34), instead of between two water molecules. Therefore, aggregation can be described in terms of $[Si(26)F_6]^{2-}$ and $[Si(19)F_6]^{2-}$ anions interconnecting $[H_7O_3]^+$ ions. The second four-membered ring is completed by two crystallographically distinct water molecules, a hydronium ion and one $[Si(26)F_6]^{2-}$ anion. In this ring, the hydronium ion (O35) serves as a H-bond donor toward F29, the water molecule (O34), and a water molecule (O34) acts as an H-bond donor toward the second water molecule (O33), and the water molecule (O33) acts as a H-bond donor toward F32 of the $[Si(26)F_6]^{2-}$ anion. The H-bonding environment of different water molecules and a hydronium ion is highlighted in Figure 23, and detailed H-bonding parameters are provided in Table S2. Next, the 16-membered cyclic motifs comprise crystallographically distinct water molecules, hexafluorosilicate anions, and hydronium ion units, creating a supramolecular assembly that propagates along the b-axis.

Apart from O−H···F interactions, anions are engaged with cationic ligands via N−H···F contacts. The $[Si(26)F_6]^{2-}$ anion reveals the bicoordinated nature of H-bonding acceptance of one fluoride atom (F27) and in total binds two cationic ligands via protonated pyridyls (N10−H10···F27 and N16−H16···F27 contacts) with the formation of $C_2^1(14)$ H-bonded zig-zag chains parallel to the a-axis. In contrast, the second

https://doi.org/10.1021/acs.cgd.3c00393
Cryst. Growth Des. 2023, 23, 5144−5162

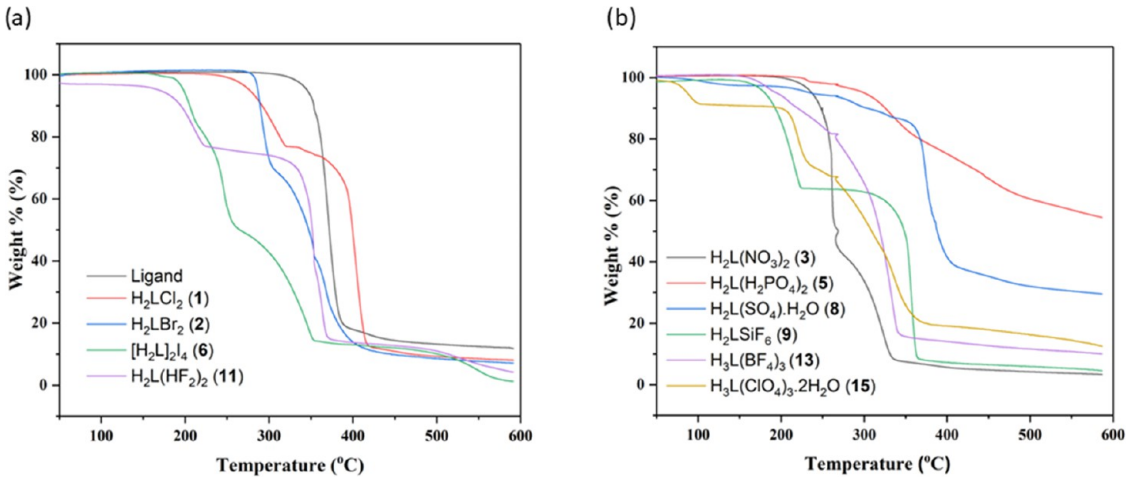

Figure 24. TG curves of the (a) ligand **L**, H_2LCl_2 (**1**), H_2LBr_2 (**2**), $[H_2L]_2I_4$ (**6**), and $H_2L(HF_2)_2$ (**11**) and (b) $H_2L(NO_3)_2$ (**3**), $H_2L(H_2PO_4)_2$ (**5**), $H_2L(SO_4)\cdot H_2O$ (**8**), H_2LSiF_6 (**9**), $H_3L(BF_4)_3$ (**13**), and $H_3L(ClO_4)_3\cdot 2H_2O$ (**15**).

hexafluorosilicate $[Si(19)F_6]^{2-}$ anion accepts three H bonds from three cationic ligands out of which two are contributed by an amino group, such that the $C_2^2(6)$ H-bonded chain is formed, which is mediated via two trans-fluoride ligands (N6−H6A···F25 and N6−H6B···F20) parallel to the *b*-axis. The third H bond is assisted by triazole nitrogen (N3) and facilitates the generation of $C_2^2(9)$ H-bonded linear chains mediated by *cis*-fluoride ligands (N6−H6A···F25Si(19)F23···H3−N3), running along the $C_2^2(6)$ H-bonded chains. As a result, bilayer arrangement is sustained by intermolecular H-bond interactions when viewed down the *b*-axis. The molecular packings along the *a*-, *b*-, and *c*-axes are shown in Figure S11. Additionally, anion−π interactions further contribute to the strengthening of the hydrogen bonding-driven assembly. The triazole ring establishes anion−π interactions involving both crystallographically distinct hexafluorosilicate anions with the fluorine atoms F21 and F32 of the $[Si(19)F_6]^{2-}$ and $[Si(26)F_6]^{2-}$ anions being only 2.7913(13) and 2.7690(13) Å apart from the ring centroid, respectively (Figure S11).

3.3. Thermogravimetry. Thermogravimetric analyses were made to examine and compare the thermal stability of the ligand and the prepared salts at 10 °C/min under a N_2 flow. As shown in Table S4 and Figure 24, the neutral ligand **L** has an onset decomposition temperature of 328 °C, and all of the examined salts illustrate decomposition temperatures between 154 and 240 °C, with salt (**11**) having the lowest and salt (**2**) the highest decomposition temperature. The observed decomposition temperatures and the corresponding weight losses indicate that the (first dehydrated in the case of hydrates) salts demonstrate the decomposition of anions as a free acid, followed by the formation of volatile products in the first stage. For instance, chloride and bromide salts underwent three prominent rapid weight losses, where the first step ended at around 283 and 270 °C with a weight loss of about 23.58 wt % (calcd. 23%) and 33.08 wt % (calcd. 40%) owing to the expected formation of volatile products such as HCl and HBr, respectively. The following weight loss corresponds to the decomposition of the ligand **L** itself, which is analogous to the behavior seen for the other halide salts (Figure 24). Regarding thermal stability, halide salts exhibited pronounced differences showing a gradual decline with the sequence of bromide, chloride, iodide, and fluoride.

The TG curve of $H_2L(NO_3)_2$ (**3**) demonstrates a sharp mass loss (58 wt %) at 159−273 °C corresponding to exothermic decomposition. This can be the result of the decomposition of nitrate anion $[NO_2 + 1/2H_2O + 1/4O_2$ (20%)]. Nevertheless, at this temperature range, there are combinations of changes occurring as a byproduct of some chemical process accompanied by effusion of the gaseous species. Complex $H_2L(H_2PO_4)_2$ (**5**) experienced gentle descending weight loss (2.15 wt %) corresponding to an endothermic reaction, which ended at around 237 °C, suggesting that this originates from surface-bound water, which is also consistent with aggregable EA results indicating the presence of a single water molecule. As shown in Figure 24, there is no clear-cut plateau on the TG curve of salt (**5**), hence deducing plausible polymerization of dihydrogen phosphate ions. The TG curve of salt $H_2L(SO_4)\cdot H_2O$ (**8**) displays a weight loss of 2.45 and 2.92 wt % (calcd. 5.07%) in two steps, originating from a loss of the water molecule in the temperature range of 62−140 and 140−242 °C, respectively. It can be speculated that the relatively high release temperature observed for the water molecule can be attributed to the strong H-bonding interactions by two sulfate anions involved in a cyclic sulfate−water cluster, which was shown in the single-crystal structure. The salt H_2LSiF_6 (**9**) shows the first weight loss of about 35.41 wt % (calcd. 37.67%) up to 231 °C corresponding to an endothermic reaction, which can be ascribed to the decomposition of a $[SiF_6]^{2-}$ anion. This is then followed by the thermal decomposition of the neutral ligand. The observed results are consistent with both crystallographic and elemental analysis results. The hydrated salt $H_3L(ClO_4)_3\cdot 2H_2O$ (**15**) decomposes in four stages of which the first step occurs in the temperature range of 44−104 °C, with a weight loss of about 7.92 wt % (calcd. 6.25%) corresponding to the release of crystal water and surface moisture. This is then followed by the initiation (onset 206 °C) of exothermic decomposition that ends at around 244 °C. The final two weight losses occurring in the temperature range of 244−375 °C (50.17 wt %) and 375−588 °C (7.51 wt %), respectively, correspond to the decomposition of the remaining ligand. Note that, as indicated by TG/DSC graphs, no melting points were observed before decomposition for all of the salts. Among the examined salts, H_2LBr_2 (**2**) salt shows the highest decomposition temperature, which is close to 240 °C. $H_2L(HF_2)_2$ (**11**), $H_3L(BF_4)_3$ (**13**), and H_2LSiF_6 (**9**) display

https://doi.org/10.1021/acs.cgd.3c00393
Cryst. Growth Des. 2023, 23, 5144−5162

the lowest thermal stability, which is <163 °C. Chloride-, iodide-, nitrate-, sulfate-, phosphate-, and perchlorate-based salts demonstrated onset decomposition temperatures in the intermediate range, which is >163 and <240 °C and can be assembled in the following series: $H_2L(HF_2)_2$ < (**11**) $H_3L(BF_4)_3$ (**13**) < H_2LSiF_6 (**9**) < $[H_2L]_2I_4$ < (**6**) $H_2L(SO_4)\cdot H_2O$ (**8**) < $H_3L(ClO_4)_3\cdot 2H_2O$ (**15**) < $H_2L(NO_3)_2$ (**3**) ≈ H_2LCl_2 (**1**) < $H_2L(H_2PO_4)_2$ (**5**) < H_2LBr_2 (**2**). All of the thermal analysis results are presented in Table S4 for comparison.

3.4. Powder X-ray Diffraction Methods (PXRD). For the most part, the Pawley refinement of the lattice parameters for each of the bulk powders was determined to be structurally analogous to the respective single-crystal structures. The fitted diffraction graphs, refined unit cells, and resulting R-factors/goodness-of-fits are shown in Figures S12−S21 and Table S5, respectively. According to obtained results, phase purity of the powder samples at all three different concentrations was confirmed for H_2LCl_2 (**1**), H_2LBr_2 (**2**), and $[H_2L]_2I_4$ (**6**). In the case of nitrate, where both monoclinic and triclinic structure modifications were obtained, the PXRD analysis clearly indicates that the bulk material corresponds to the monoclinic $H_2L(NO_3)_2$ (**3**) salt in 2.5 and 5 M concentrations used in the reactions. However, with a low concentration (1 M), along with the major monoclinic product, some unreacted ligands remained as well, indicating that milder 1 M HNO_3 is not sufficient to fully protonate the ligand within the tested reaction conditions (Figure S14). For both phosphate structures, displaying either mono- or diprotonated ligand with one or two dihydrogen phosphate anions (**4**, **5**), the PXRD analysis confirmed that the bulk powder corresponds to the $H_2L(H_2PO_4)_2$ (**5**) salt in all three different concentrations.

The biggest differences between single crystals and their corresponding bulk powders were witnessed for the $H_2L(SO_4)\cdot H_2O$ (**8**) and $H_2L(HF_2)_2$ (**11**). For the salt (**8**), powders resulting from the tested acid concentrations differed significantly. The PXRD pattern of the powder product yielded from a 1 M solution corresponds somewhat well to the simulated pattern of the single-crystal data. The powder product obtained from a 2.5 M acid concentration contained a trace amount of a polymorph. However, the pattern measured from the 5 M concentration was completely different from the expected simulated patterns and can be assumed to be either some polymorph of the sulfate salt or hydrogen sulfate salt, agreeably confirmed with elemental analysis results. For crystal structure $H_2L(HF_2)_2$ (**11**), based on the Pawley fit, all three acid concentrations resulted in bulk powders consisting merely of the neutral ligand, which was also confirmed by the elemental analysis. This could be possibly attributed to the weak acidic nature of the acid, ligand neutralization, or salt instability. For the salt $H_3L(BF_4)_3$ (**13**), the powder product obtained from a 1 M acid concentration contained a trace amount of some unknown impurity, which does not match the simulated pattern or the PXRD pattern of the neutral ligand. However, the bulk products obtained at other concentrations (2.5 and 5 M) were structurally similar to the single-crystal X-ray structure of salt (**13**), as shown in Figure S20. The best Pawley fits were made with H_2LSiF_6 (**9**) and $H_3L(ClO_4)_3$ (**14**), as the PXRD patterns from all three acid concentrations match the corresponding single-crystal structures.

4. CONCLUSIONS

In this study, we have focused on designing new anion-templated supramolecular assemblies of the bent 4-amino-3,5-bis(4-pyridyl)-1,2,4-triazole ligand constituting distinct H-bonded geometry ring [$R_2^2(8)$, $R_2^4(8)$, $R_4^4(20)$, $R_4^4(24)$, and $R_4^4(28)$] and chain [$C_1^1(5)$, $C_2^1(10)$, $C_2^1(14)$, $C_2^2(6)$, $C_2^2(9)$, $C_2^2(11)$, $C_2^2(12)$, $C_2^2(16)$] patterns. We explored how subtle modulation in a crystallization environment and conditions offers the possibility to yield entirely different forms of molecular salts with mono-, di-, or triprotonated ligands. Three significantly different conformations of these 16 molecular salts were differentiated, and the influence of anion's steric effects on the molecular conformations suggested that steric hindrance provided by the polyhedron conformation of anions accounts for the twisted conformation of the ligand. On the other hand, ligands showcased better planarity with smaller spherical anions (Cl^- and Br^-), with strong $\pi-\pi$ interactions (bricklayer fashion) further reinforcing the molecular packing. With in-depth studies on the crystal structures, we were able to unveil some key structural aspects of hexameric anion cluster assembly $[(H_2PO_4^-)_6]$ of the $R_6^6(24)$ motif and anion−water clusters ranging from a cyclic tetramer $[(SO_4)_2-(H_2O)_2]^{4-}$ of the $R_4^4(12)$ motif and an octameric cluster $[(SiF_6)_4-(H_2O)_4]_\infty^{8-}$ of the $R_8^8(24)$ structural motif to an acyclic tetramer $[(ClO_4^-)_2(H_2O)_2]$.

Focusing on intrinsic anion chemistry, we demonstrate key structural insights into vast and varied ranging supramolecular networks of the bent ligand manifested by a synergistic interplay of multiple noncovalent interactions with a panel of different anion geometries ranging from linear ($[HF_2]^-$), spherical (Cl^-, Br^-, I^-), trigonal planar ($[NO_3]^-$), and tetrahedral ($[ClO_4]^-$, $[SO_4]^{2-}$, $[H_2PO_4]^-$, $[BF_4]^-$) to octahedral ($[SiF_6]^{2-}$). The hydrogen bonding-driven assemblies alongside anion−π interactions and $\pi-\pi$ stacking emerged as key players in establishing entirely diverse supramolecular entities, distinctive H-bonded motifs, and intriguing anion−water clusters. Thus, this work with detailed examples of specific inorganic anions warrants the relevant information associated with the rational design of anion-mediated supramolecular entities and aids in understanding how the coexistence of different noncovalent interactions mutually influences the supramolecular systems. Indeed, insights obtained can be grasped to acquire a wider understanding of new families of synthetic molecular systems and leverage the application of noncovalent interactions as a supramolecular tool to manipulate preferred binding systems for the complexation of a particular anion.

■ ASSOCIATED CONTENT

Supporting Information

The Supporting Information is available free of charge at https://pubs.acs.org/doi/10.1021/acs.cgd.3c00393.

^{1}H NMR and ^{13}C NMR spectra; FTIR spectroscopy; molecular conformations; crystallographic data; hydrogen-bonding distances (Å) and bond angles (deg); geometric parameters $d_{centroid}$, d_{plane}, and d_{offset}; partial view of molecular packing; thermogravimetric results; Pawley analysis of bulk powders; percent yields of bulk powders; and Pawley refinement plots (PDF)

Accession Codes

CCDC 2252716−2252731 contain the supplementary crystallographic data for this paper. These data can be obtained

https://doi.org/10.1021/acs.cgd.3c00393
Cryst. Growth Des. 2023, 23, 5144−5162

free of charge via www.ccdc.cam.ac.uk/data_request/cif, or by emailing data_request@ccdc.cam.ac.uk, or by contacting The Cambridge Crystallographic Data Centre, 12 Union Road, Cambridge CB2 1EZ, UK; fax: +44 1223 336033.

AUTHOR INFORMATION

Corresponding Author

Manu Lahtinen − *Department of Chemistry, University of Jyväskylä, FI-40014 Jyväskylä, Finland;* orcid.org/0000-0001-5561-3259; Email: manu.k.lahtinen@jyu.fi

Authors

Shreya Mahajan − *Department of Chemistry, University of Jyväskylä, FI-40014 Jyväskylä, Finland*

Antti Marttinen − *Department of Chemistry, University of Jyväskylä, FI-40014 Jyväskylä, Finland*

Samu Forsblom − *Department of Chemistry, University of Jyväskylä, FI-40014 Jyväskylä, Finland*

Complete contact information is available at: https://pubs.acs.org/10.1021/acs.cgd.3c00393

Notes

The authors declare no competing financial interest.

ACKNOWLEDGMENTS

This study was financially supported by the Academy of Finland (Decision Number 329314) and the University of Jyväskylä.

REFERENCES

(1) Lehn, J.-M. From Supramolecular Chemistry towards Constitutional Dynamic Chemistry and Adaptive Chemistry. *Chem. Soc. Rev.* **2007**, *36*, 151−160.

(2) Plais, R.; Boufroura, H.; Gouarin, G.; Gaucher, A.; Haldys, V.; Brosseau, A.; Clavier, G.; Salpin, J. Y.; Prim, D. Design and Property Investigation on a Five-Interaction-Based Fluorescent Anion Receptor Clip. *RSC Adv.* **2021**, *11*, 9476−9487.

(3) Plais, R.; Gouarin, G.; Bournier, A.; Zayene, O.; Mussard, V.; Bourdreux, F.; Marrot, J.; Brosseau, A.; Gaucher, A.; Clavier, G.; Salpin, J.; Prim, D. Chloride Binding Modulated by Anion Receptors Bearing Tetrazine and Urea. *ChemPhysChem* **2023**, *24*, No. 2200524.

(4) Molina, P.; Zapata, F.; Caballero, A. Anion Recognition Strategies Based on Combined Noncovalent Interactions. *Chem. Rev.* **2017**, *117*, 9907−9972.

(5) Li, H.; Valkenier, H.; Thorne, A. G.; Dias, C. M.; Cooper, J. A.; Kieffer, M.; Busschaert, N.; Gale, P. A.; Sheppard, D. N.; Davis, A. P. Anion Carriers as Potential Treatments for Cystic Fibrosis: Transport in Cystic Fibrosis Cells, and Additivity to Channel-Targeting Drugs. *Chem. Sci.* **2019**, *10*, 9663−9672.

(6) Yamada, S. Cation−π Interactions in Organic Synthesis. *Chem. Rev.* **2018**, *118*, 11353−11432.

(7) Chifotides, H. T.; Dunbar, K. R. Anion−π Interactions in Supramolecular Architectures. *Acc. Chem. Res.* **2013**, *46*, 894−906.

(8) Janiak, C. A Critical Account on π−π Stacking in Metal Complexes with Aromatic Nitrogen-Containing Ligands. *J. Chem. Soc., Dalton Trans.* **2000**, *21*, 3885−3896.

(9) Peuronen, A.; Valkonen, A.; Kortelainen, M.; Rissanen, K.; Lahtinen, M. Halogen Bonding-Based "Catch and Release": Reversible Solid-State Entrapment of Elemental Iodine with Monoalkylated DABCO Salts. *Cryst. Growth Des.* **2012**, *12*, 4157−4169.

(10) Xia, X.; Zhang, S.; Li, S.; Zhang, L.; Wang, G.; Zhang, L.; Wang, J.; Li, Z. The Cycle of Nitrogen in River Systems: Sources, Transformation, and Flux. *Environ. Sci.: Processes Impacts* **2018**, *20*, 863−891.

(11) Eytel, L. M.; Fargher, H. A.; Haley, M. M.; Johnson, D. W. The Road to Aryl CH···anion Binding Was Paved with Good Intentions: Fundamental Studies, Host Design, and Historical Perspectives in CH Hydrogen Bonding. *Chem. Commun.* **2019**, *55*, 5195−5206.

(12) Mahadevi, A. S.; Sastry, G. N. Cooperativity in Noncovalent Interactions. *Chem. Rev.* **2016**, *116*, 2775−2825.

(13) Custelcean, R. Anions in Crystal Engineering. *Chem. Soc. Rev.* **2010**, *39*, 3675−3685.

(14) Hoque, M. N.; Das, G. Overview of the Strategic Approaches for the Solid-State Recognition of Hydrated Anions. *CrystEngComm* **2017**, *19*, 1343−1360.

(15) Hossain, M. A.; Işiklan, M.; Pramanik, A.; Saeed, M. A.; Fronczek, F. R. Anion Cluster: Assembly of Dihydrogen Phosphates for the Formation of a Cyclic Anion Octamer. *Cryst. Growth Des.* **2012**, *12*, 567−571.

(16) Chutia, R.; Dey, S. K.; Das, G. Self-Assembly of a Tris(Urea) Receptor as Tetrahedral Cage for the Encapsulation of a Discrete Tetrameric Mixed Phosphate Cluster $(H_2PO_4^-{\cdot}HPO_4^{2-})_2$. *Cryst. Growth Des.* **2015**, *15*, 4993−5001.

(17) Hoque, M. N.; Das, G. Cationic Tripodal Receptor Assisted Formation of Anion and Anion-Water Clusters: Structural Interpretation of Dihydrogen Phosphate Cluster and Sulfate-Water Tetramer $[(SO_4)_2{-}(H_2O)_2]^{4-}$. *Cryst. Growth Des.* **2014**, *14*, 2962−2971.

(18) Pramanik, S.; Thordarson, P.; Day, V. W.; Bowman-James, K. Oligomeric Phosphate Clusters in Macrocyclic Channels. *CrystEngComm* **2022**, *24*, 8047−8051.

(19) He, Q.; Tu, P.; Sessler, J. L. Supramolecular Chemistry of Anionic Dimers, Trimers, Tetramers, and Clusters. *Chem* **2018**, *4*, 46−93.

(20) White, N. G. Antielectrostatically Hydrogen Bonded Anion Dimers: Counter-Intuitive, Common and Consistent. *CrystEngComm* **2019**, *21*, 4855−4858.

(21) Zhao, W.; Flood, A. H.; White, N. G. Recognition and Applications of Anion−Anion Dimers Based on Anti-Electrostatic Hydrogen Bonds (AEHBs). *Chem. Soc. Rev.* **2020**, *49*, 7893−7906.

(22) Gale, P. A.; Howe, E. N. W.; Wu, X.; Spooner, M. J. Anion Receptor Chemistry: Highlights from 2016. *Coord. Chem. Rev.* **2018**, *375*, 333−372.

(23) Jagleniec, D.; Dobrzycki, Ł.; Karbarz, M.; Romański, J. Ion-Pair Induced Supramolecular Assembly Formation for Selective Extraction and Sensing of Potassium Sulfate. *Chem. Sci.* **2019**, *10*, 9542−9547.

(24) Beckendorf, S.; Asmus, S.; Mancheño, O. G. H-Donor Anion Acceptor Organocatalysis-The Ionic Electrophile Activation Approach. *ChemCatChem* **2012**, *4*, 926−936.

(25) Coles, M. P. Bicyclic-Guanidines, -Guanidinates and -Guanidinium Salts: Wide Ranging Applications from a Simple Family of Molecules. *Chem. Commun.* **2009**, *25*, 3659.

(26) Busschaert, N.; Caltagirone, C.; Van Rossom, W.; Gale, P. A. Applications of Supramolecular Anion Recognition. *Chem. Rev.* **2015**, *115*, 8038−8155.

(27) Liu, T. P.; Huo, L. H.; Deng, Z. P.; Zhao, H.; Gao, S. Supramolecular Architectures and Luminescent Properties of the Salts Containing Flexible Bis(Pyridyl) Cations with Aliphatic Diamine Spacer: Effects of Inorganic Anions, Alkalinity and Conformation of the Bis(Pyridyl) Cations. *RSC Adv.* **2014**, *4*, 40693−40710.

(28) Zhang, Z.-Y.; Deng, Z.-P.; Huo, L.-H.; Zhao, H.; Gao, S. Inorganic Anion Induced Supramolecular Architectures of Flexible Unsymmetrical Bis(Pyridyl) Ionic Salts Mediated by Various Non-Covalent Interactions. *CrystEngComm* **2013**, *15*, 5261.

(29) Ding, X.-H.; Wang, S.; Li, Y.-H.; Huang, W. Inorganic Anion-Assisted Supramolecular Assemblies of Bent Dipyridines: Effects of Anionic Geometries on Hydrogen-Bonding Networks. *Inorg. Chem. Front.* **2015**, *2*, 263−272.

(30) Roubeau, O. Triazole-Based One-Dimensional Spin-Crossover Coordination Polymers. *Chem. − Eur. J.* **2012**, *18*, 15230−15244.

(31) Dupouy, G.; Marchivie, M.; Triki, S.; Sala-Pala, J.; Gómez-García, C. J.; Pillet, S.; Lecomte, C.; Létard, J.-F. Photoinduced HS

State in the First Spin-Crossover Chain Containing a Cyanocarbanion as Bridging Ligand. *Chem. Commun.* **2009**, *23*, 3404.
(32) White, N. G.; Brooker, S. Metal Acetates Form Diverse Polynuclear Complexes with 4-Amino-3,5-Di(2-Pyridyl)-1,2,4-Triazole (Adpt). *Supramol. Chem.* **2013**, *25*, 806−811.
(33) White, N. G.; Kitchen, J. A.; Brooker, S. A Structural Investigation of Anion−Triazole Interactions: Observation of "Π-Pockets" and "Π-Sandwiches.". *Eur. J. Inorg. Chem.* **2009**, *2009*, 1172−1180.
(34) Qin, B.; Zhang, X.; Zhang, J. A New Multifunctional Zinc−Organic Framework with Rare Interpenetrated Tripillared Bilayers as a Luminescent Probe for Detecting Ni^{2+} and PO_4^{3-} in Water. *Cryst. Growth Des.* **2020**, *20*, 5120−5128.
(35) Lee, L.-W.; Kao, Y.-C.; Chung, M.-Y.; Chang, B.-C.; Lee, G.-H.; Peng, S.-M.; Wang, C.-M.; Liu, Y.-H.; Lee, S.-L.; Lu, K.-L. Rare Metal-Ion Metathesis of a Tetrahedral Zn(II) Core of a Noncentrosymmetric (3,4)-Connected 3D MOF. *Dalton Trans.* **2019**, *48*, 1950−1954.
(36) Chatterjee, N.; Oliver, C. L. A Dynamic, Breathing, Water-Stable, Partially Fluorinated, Two-Periodic, Mixed-Ligand Zn(II) Metal−Organic Framework Modulated by Solvent Exchange Showing a Large Change in Cavity Size: Gas and Vapor Sorption Studies. *Cryst. Growth Des.* **2018**, *18*, 7570−7578.
(37) Mahajan, S.; Lahtinen, M. Recent Progress in Metal-Organic Frameworks (MOFs) for CO_2 Capture at Different Pressures. *J. Environ. Chem. Eng.* **2022**, *10*, No. 108930.
(38) Du, M.; Jiang, X.-J.; Tan, X.; Zhang, Z.-H.; Cai, H. Co-Crystallization of a Versatile Building Block 4-Amino- 3,5-Bis(4-Pyridyl)-1,2,4-Triazole with R-Isophthalic Acids (R = −H, $-NH_2$, $-SO_3H$, and −COOH): Polymorphism and Substituent Effect on Structural Diversity. *CrystEngComm* **2009**, *11*, 454−462.
(39) *CrysAlisPRO*; Oxford Diffraction/Agilent Technologies UK Ltd.: Yarnton, England.
(40) Sheldrick, G. M. SHELXT - Integrated Space-Group and Crystal-Structure Determination. *Acta Crystallogr., Sect. A* **2015**, *71*, 3−8.
(41) Sheldrick, G. M. Crystal Structure Refinement with SHELXL. *Acta Crystallogr., Sect. C* **2015**, *71*, 3−8.
(42) Dolomanov, O. V.; Bourhis, L. J.; Gildea, R. J.; Howard, J. A. K.; Puschmann, H. OLEX2: A Complete Structure Solution, Refinement and Analysis Program. *J. Appl. Crystallogr.* **2009**, *42*, 339−341.
(43) Gruene, T.; Hahn, H. W.; Luebben, A.; Meilleur, F.; Sheldrick, G. M. Refinement of Macromolecular Structures against Neutron Data with SHELXL2013. *J. Appl. Crystallogr.* **2014**, *47*, 462−466.
(44) Degen, T.; Sadki, M.; Bron, E.; König, U.; Nénert, G. The HighScore Suite. *Powder Diffr.* **2014**, *29*, S13−S18.
(45) Pawley, G. S. Unit-Cell Refinement from Powder Diffraction Scans. *J. Appl. Crystallogr.* **1981**, *14*, 357−361.
(46) Bentiss, F.; Lagrenée, M.; Traisnel, M.; Mernari, B.; Elattari, H. A Simple One Step Synthesis of New 3,5-Disubstituted-4-Amino-1,2,4-Triazoles. *J. Heterocycl. Chem.* **1999**, *36*, 149−152.
(47) Etter, M. C.; MacDonald, J. C.; Bernstein, J. Graph-set Analysis of Hydrogen-bond Patterns in Organic Crystals. *Acta Crystallogr., Sect. B* **1990**, *46*, 256−262.
(48) Savastano, M.; Bazzicalupi, C.; Giorgi, C.; García-Gallarín, C.; López De La Torre, M. D.; Pichierri, F.; Bianchi, A.; Melguizo, M. Anion Complexes with Tetrazine-Based Ligands: Formation of Strong Anion-π Interactions in Solution and in the Solid State. *Inorg. Chem.* **2016**, *55*, 8013−8024.
(49) Berryman, O. B.; Bryantsev, V. S.; Stay, D. P.; Johnson, D. W.; Hay, B. P. Structural Criteria for the Design of Anion Receptors: The Interaction of Halides with Electron-Deficient Arenes. *J. Am. Chem. Soc.* **2007**, *129*, 48−58.
(50) Kim, H.-J. Assembly of Sn(IV)-Porphyrin Cation Exhibiting Supramolecular Interactions of Anion···Anion and Anion···π Systems. *Molbank* **2022**, *2022*, M1454.
(51) Hursthouse, M. B.; Montis, R.; Niitsoo, L.; Sarson, J.; Threlfall, T. L.; Asiri, A. M.; Khan, S. A.; Obaid, A. Y.; Al-Harbi, L. M. Anhydrates and/or Hydrates in Nitrate, Sulphate and Phosphate Salts of 4-Aminopyridine, (4-AP) and 3,4-Diaminopyridine (3,4-DAP): The Role of the Water Molecules in the Hydrates. *CrystEngComm* **2014**, *16*, 2205−2219.
(52) Arunachalam, M.; Ghosh, P. A Versatile Tripodal Amide Receptor for the Encapsulation of Anions or Hydrated Anions via Formation of Dimeric Capsules. *Inorg. Chem.* **2010**, *49*, 943−951.
(53) Nath, J. K.; Baruah, J. B. Water Assisted Anion Chains and Anion Dependent Fluorescence Emission in Salts of N,N′-Bis(3-Imidazol-1-Ylpropyl)Naphthalenediimide. *New J. Chem.* **2013**, *37*, 1509−1519.
(54) Bauzá, A.; Frontera, A.; Mooibroek, T. J. NO3− Anions Can Act as Lewis Acid in the Solid State. *Nat. Commun.* **2017**, *8*, No. 14522.
(55) Franconetti, A.; Frontera, A.; Mooibroek, T. J. Intramolecular π−Hole Interactions with Nitro Aromatics. *CrystEngComm* **2019**, *21*, 5410−5417.
(56) Mooibroek, T. J. Coordinated Nitrate Anions Can Be Directional π-Hole Donors in the Solid State: A CSD Study. *CrystEngComm* **2017**, *19*, 4485−4488.
(57) Bauzá, A.; Frontera, A.; Mooibroek, T. J. Π-Hole Interactions Involving Nitro Aromatic Ligands in Protein Structures. *Chem. − Eur. J.* **2019**, *25*, 13436−13443.
(58) Zhang, G.; Zhang, X.; Kong, L.; Wang, S.; Tian, Y.; Tao, X.; Yang, J. Anion-Controlled Dimer Distance Induced Unique Solid-State Fluorescence of Cyano Substituted Styrene Pyridinium. *Sci. Rep.* **2016**, *6*, No. 37609.
(59) Mahé, N.; Nicolaï, B.; Allouchi, H.; Barrio, M.; Do, B.; Céolin, R.; Tamarit, J. L.; Rietveld, I. B. Crystal Structure and Solid-State Properties of 3,4-Diaminopyridine Dihydrogen Phosphate and Their Comparison with Other Diaminopyridine Salts. *Cryst. Growth Des.* **2013**, *13*, 708−715.
(60) Gelmboldt, V. O.; Ganin, E.; Fonari, M. S.; Simonov, Y. A.; Koroeva, Lv.; Ennan, A. A.; Basok, S. S.; Shova, S.; Kählig, H.; Arion, V. B.; Keppler, B. K. Two New "Onium" Fluorosilicates, the Products of Interaction of Fluorosilicic Acid with 12-Membered Macrocycles: Structures and Spectroscopic Properties. *Dalton Trans.* **2007**, *27*, 2915−2924.
(61) Hoque, M. N.; Manna, U.; Das, G. Discrepancy in Anion Coordination Directed by Isomeric Pyridine−Urea Receptors: Solid State Recognition of Hydrated Anions. *Polyhedron* **2016**, *119*, 307−316.

https://doi.org/10.1021/acs.cgd.3c00393
Cryst. Growth Des. 2023, 23, 5144−5162